MASTER

Cold atom dynamics in a magnetic trap

Gommers, R.

Award date:
2004

TU/e technische universiteit eindhoven

Eindhoven University of Technology,
Department of Applied Physics,
Experimental Atomic Physics and Quantum Electronics Group.

Cold Atom Dynamics in a Magnetic Trap

R. Gommers

Graduation report
AQT/B 04-01
January 2004

Guidance: Ir. B.J. Claessens,
Dr. ir. E.J.D. Vredenbregt,
Prof. dr. H.C.W. Beijerinck.

Summary

In this thesis experimental as well as theoretical work aimed at understanding the dynamics of a gas of cold neon atoms in a magnetic trap is described. The focus of the experimental work has been on obtaining more atoms in the trap at a lower temperature in a reliable way. To that end the experimental setup has been improved by making the optical system more stable and the pressure in the vacuum system lower. Spin polarization of the atoms has enabled efficient transfer of atoms from a magneto-optical trap to a magnetic trap, obtaining approximately 10^9 atoms in the magnetic trap. Optical molasses experiments have resulted in a temperature of the atom cloud in the magnetic trap of about 950μK.

Two different methods to determine the cross-section σ for elastic collisions have been examined. For the two knives experiment, based on observing the redistribution of atoms in energy space after the most energetic atoms have been removed by radio-frequency radiation, the number of collisions needed to obtain a thermal Boltzmann distribution is determined. It is found that under current experimental conditions this method will not be able to yield a reliable value for σ.

A more promising method is the observation of the relaxation of the atom cloud towards equilibrium after the shape of the magnetic trap is changed. This method will be able to yield a value for σ if the temperature of the atom cloud can be reduced to below 400μK, which is attainable by implementing a new optical cooling technique in the magnetic trap. This temperature is found to be determined by anharmonic mixing, a phenomenon that can cause the relaxation to take place without collisions. An elaborate characterization of the timescales on which anharmonic mixing takes place is given. An experiment in which relaxation of the atom cloud was observed is explained by anharmonic mixing. When determining the mixing timescales, an interesting resonance in it was found at a ratio of radial and axial trap frequencies of $3:2$. A qualitative model, based on Birkhoff-Gustavson normalization of the potential of the magnetic trap, explains the position of this resonance.

Acknowledgements

The year I have spent working in the AQT group has been very enjoyable, and I have a lot of people to thank for that. First of all I would like to thank Bert Claessens for a very pleasant collaboration. Our endless discussions have also been really motivating and have forced me to really get to the bottom of the problems we encountered. And as a bonus I got to find out from him how our Belgian neighbors really feel about us Dutchmen.

I want to thank my supervisor Edgar Vredenbregt as well, his door was always open to discuss whatever was on my mind. And I think the good atmosphere in our team had a lot to do with his humor and positive attitude.

My two Australian coworkers Jonathan Ashmore and Colin Hawthorn have helped me out a lot in the lab during their stays here and I thank both of them for that.

I also thank Herman Beijerinck for always trying to look at problems from another perspective and stimulating me to see the bigger picture.

The group's technicians Jolanda van de Ven and Louis van Moll helped me out a lot with my work on the vacuum system, thanks to both of you. I also appreciated the valuable additional technical support from Rein Romphorst, who helped me win my fight with a box full of electronics and along the way provided me with some unsolicited but very welcome humorous life lessons.

Last but not least I want to thank my family, who I could always fall back on not only this year but also during the rest of the six years I spent here in Eindhoven.

Contents

Chapter 1

Introduction

1.1 Bose Einstein condensation

Bose Einstein condensation is a phenomenon that was predicted as early as 1924 by Bose and Einstein [1, 2]. The first experiments aimed at creating a condensate were done with liquid helium and with a cold hydrogen gas. These experiments, combined with the development of laser cooling and trapping techniques, laid the foundation for the experiments with alkali atoms that led to the first experimental observations of a Bose Einstein condensate (BEC) in 1995 [3, 4]. The condensation is a phase transition that occurs in atomic gases when they are cooled down to the transition point, where the interatomic distance is of the order of the thermal de Broglie wavelength. The transition point is defined by a phase space density of:

$$n_0 \lambda_{dB}^3 = 2.612, \tag{1.1}$$

where n_0 is the central atomic density and λ_{dB} is the de Broglie wavelength. The condensate consists of atoms that are all in the lowest energy state. Only bosons can be condensed this way, fermions obey the Pauli exclusion principle and can therefore not all be in the lowest energy state.

The atoms that have been used to create condensates until now are ^{87}Rb [4], ^{23}Na [3], ^{85}Rb [5], ^{7}Li [6], ^{1}H [7], ^{4}He* [8], ^{41}K [9], ^{133}Cs [10] and ^{174}Yb [11]. All these species have their specific properties, such as an interaction strength tunable by a magnetic field for several species, a large internal energy for ^{4}He* or the absence of spin for ^{174}Yb. Very recently molecular condensates have also been created with $^{6}Li_2$ [12] and $^{40}K_2$ [13]. The large interest in BEC research is explained by the possible applications, that range from studying quantum statistics to atom interference experiments to the creation of an atom laser, the equivalent of an optical laser with matter waves. The experiments that are done at the Eindhoven University of Technology are aimed at creating a BEC of metastable neon. Metastable neon has a large internal energy of 16eV which allows single atom detection, a large advantage compared to alkali atoms. It is much harder to work with however, due to the limited lifetime of the metastable state of 14.7s [14], a large two-body loss rate due

to the large internal energy that can be released in a collision and the low efficiency of $10^{-4} - 10^{-5}$ of the production of metastable atoms from a discharge source.

Producing a $^{20}Ne^*$ BEC is basically a three-step procedure [15]. First, a magneto-optical trap (MOT) has to be loaded from an atomic beam. This step is routinely performed in the lab now, up to 10^9 atoms can be trapped at a temperature of about 1mK. The second step is to transfer those atoms from the MOT to a magnetic trap (MT). This can also be done now with an efficiency close to unity. The last step is to cool the atoms in the MT to the point where Bose Einstein condensation begins, which is typically at a temperature of about 1μK for 10^6 atoms. At the moment this has not been achieved.

1.2 Magneto-Optical Trapping

Magneto-optical trapping of neutral atoms is the most applied technique to obtain atomic clouds with temperatures below 1mK [16]. The main reasons are that a MOT is not very sensitive to variations in alignment, polarization and intensity of the trapping laser beams and that a MOT is able to efficiently capture atoms over a large velocity range. The MOT operates on a closed optical transition, which for Ne* is the $^3P_2 \rightarrow ^3D_3$ transition at a wavelength of 640.224nm. The linewidth of the transition is $\Gamma = 8.2 \cdot (2\pi)$MHz. The MOT consists of a spherical quadrupole magnetic field and three pairs of mutually orthogonal counterpropagating $\sigma^+ - \sigma^-$ polarized laser beams. These beams are red detuned, meaning that the frequency of the light ω_l is smaller than the frequency of the atomic transition ω_a. The detuning δ is defined as $\delta = \omega_l - \omega_a$. The atoms in the MOT experience a force because they absorb light from the laser beams and re-emit that light spontaneously. The force from each beam is given by:

$$F = \frac{\hbar k s_0 \Gamma/2}{1 + s_0 + (2\delta/\Gamma)^2}, \tag{1.2}$$

where k is the wavevector of the light and $s_0 = I/I_s$ is the saturation parameter, with I the light intensity and I_s the saturation intensity of the atom. The force from the three pairs of beams together is directed to the center of the trap because the energy levels of the atom are Zeeman shifted in such a way that they scatter more light from the laser beam that is directed towards the center of the trap than from the one that is directed away from it. The MOT configuration and the principle of the position-dependent trapping force are shown in Figure 1.1.

The number of atoms that the MOT can contain depends on the loading rate of the atomic beam, the losses due to collisions with background atoms and the two-body losses:

$$\frac{dN}{dt} = R - \frac{N}{\tau_{bg}} - \frac{\beta}{V} N^2, \tag{1.3}$$

where R is the loading rate, τ_{bg} the trap lifetime due to collisions with the background gas, β the two-body loss rate and V the trap volume. The lowest temperature of the atom cloud that can be reached in the MOT is the Doppler temperature $T_D = \frac{\hbar\Gamma}{2k_B}$, because the

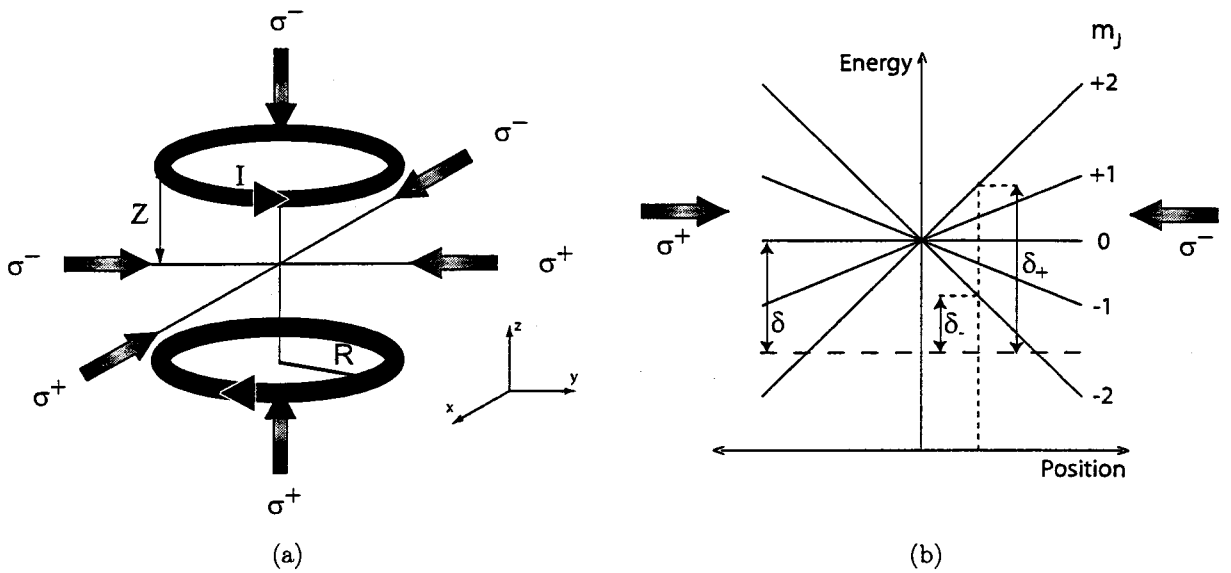

Figure 1.1: *a) Artists impression of the MOT configuration, with the two coils and three pairs of counterpropagating $\sigma_+ - \sigma^-$ laser beams. b) Energy diagram for the magnetic sub-states of the atom in the MOT and the laser beams. The effective detunings δ_+, δ_- for the respective beams show that the beam directed towards the center of the trap is always closer to resonance and therefore more photons from this beam will be scattered by the atom.*

interaction of the atoms with the laser beams causes a heating rate due to spontaneous emission of absorbed photons. Therefore the MOT is only suited for the accumulation of atoms, not for cooling them further towards the BEC transition temperature. For neon the Doppler temperature is 203μK.

1.3 Magnetic Trapping

Because the atoms possess a magnetic moment they can be trapped by a magnetic field. In a magnetic trap there is no lower limit to the temperature that can be reached, contrary to the MOT. The trapping force of the MT is given by:

$$\vec{F} = -\nabla(\vec{\mu} \cdot \vec{B}) = -m_J \mu_B g_J \nabla B, \tag{1.4}$$

where $\vec{\mu}$ is the magnetic moment of the atom, m_J is the magnetic quantum number, μ_B is the Bohr magneton and g_J is the Landé factor. From this expression it can be seen that an extremum in the magnetic field will be able to exert a force on an atom that is always directed towards that extremum, and will therefore be the center of the trap. The magnetic field can only possess local minima and no local maxima [17], therefore for neon only the $m_J = +1, +2$ states can be trapped. The magnetic field is generated by three

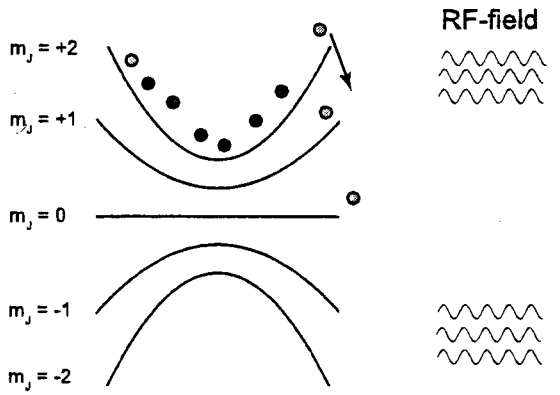

Figure 1.2: *Atoms in the $|m_J = +2\rangle$ state are trapped by a magnetic potential. The most energetic atoms can make Landau-Zener transitions with $\Delta m_J = -1$ and are not confined by the magnetic potential anymore.*

pairs of coils, giving a quadrupole field in the radial direction of the trap and a harmonic field in the axial direction. In Chapter 4 the magnetic trap will be described in detail.

1.4 Evaporative Cooling

The last step towards condensation is to cool the atoms down to the transition point. This usually can't be done by optical cooling techniques because the transition temperature is lower than the recoil temperature $T_r = \frac{(\hbar k)^2}{2mk_B}$, where $\hbar k$ is the photon momentum, m the atomic mass and k_B the Boltzmann constant. For neon this temperature is $T_r = 2.3\mu$K. The recoil temperature is defined by the kinetic energy of an atom after a single spontaneous emission event and gives a lower limit on temperatures attainable by optical means. Evaporative cooling can be used to cool an atom cloud to below the recoil limit. The basic idea is to remove atoms from the magnetic trap that have an energy much higher than the average thermal energy. Through collisions thermal equilibrium is then restored and a lower temperature is obtained. The energy selective removal of atoms is done with a radio-frequency field. When the difference in Zeeman energy between two magnetic sub-states of an atom matches the energy of a RF-photon,

$$\Delta E_z = \mu_B g_J |\mathbf{B}(\mathbf{r})| = \hbar\omega_{rf}, \tag{1.5}$$

the atom can undergo a Landau-Zener transition [18] and reach a magnetic sub-state that is not trapped by the magnetic trap, as shown in Figure 1.2. Here μ_B is the Bohr magneton, g_J the Landé factor and ω_{rf} the frequency of the RF-field. By ramping down the RF-field at the right speed the temperature can be decreased in a continuous way.

Whether it is possible to reach the transition point by evaporative cooling depends on two parameters, the scattering length a and the Penning ionization coefficient β. The scattering length determines the collisional cross-section, $\sigma = 8\pi a^2$, and thereby the elastic

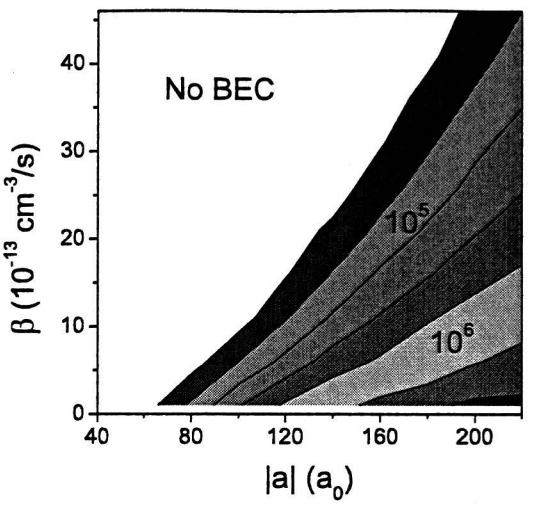

Figure 1.3: *The number of atoms that can be obtained in a BEC is shown as a function of scattering length a and Penning ionization rate β, starting from an atomic cloud with a temperature of 1mK and* 10^9 *atoms.*

collision rate. The higher this rate is, the faster rethermalization takes place. The Penning ionization coefficient determines the rate at which atoms are lost from the trap, thereby reducing the density. These two parameters determine the ratio of good to bad collisions and if this ratio is not high enough then there is a point from where on the phase space density can not be increased any more, making it impossible to reach the transition point. In Figure 1.3 is shown if a BEC of Ne^* can be made and with how many atoms as a function of a and β. The results in that Figure are obtained from a numerical simulation of the evaporative cooling process starting with an atom cloud of 10^9 atoms with a temperature of 1mK, typical values for the experiments. For metastable neon the values of a and β were unknown until very recently, when they were measured by a group in Hannover [19]. The values that were obtained are:

$$\begin{aligned} {}^{20}\text{Ne:} \quad & a = 32 \pm 6a_0, \quad \beta = 5.3 \pm 0.15 \cdot 10^{12} cm^3/s, \\ {}^{22}\text{Ne:} \quad & a = 190^{+210}_{-70} a_0, \quad \beta = 9.4 \pm 0.24 \cdot 10^{12} cm^3/s. \end{aligned} \tag{1.6}$$

Obtaining a BEC with ^{20}Ne will be nearly impossible if these measurements hold up, for ^{22}Ne there is still a chance.

The initial conditions for evaporative cooling, that is temperature and density, determine the time needed for a cooling ramp down to the transition point. Due to the finite lifetime of the metastable state [14] it is important to minimize this ramp time. Both a low initial temperature and a high initial density are important in this respect, but as usually a trade-off has to be made between the two, a rule of thumb is that a higher density is preferable to a lower temperature at equal phase space densities. The reason for this is that

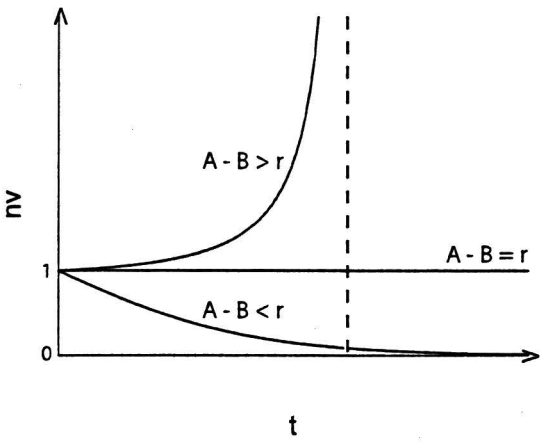

Figure 1.4: *The collision rate as a function of time in arbitrary units. The quantity r is defined as* $(\tau\Gamma_{el})^{-1}$.

the dependence of the phase space density on number of atoms N, on which the density depends linearly, and temperature T is $\sim NT^{-4}$ while the collision rate goes as $\sim NT^{-2}$, therefore the initial collision rate will be higher in the former case.

Efficient evaporative cooling will occur if the cooling process is in the "runaway" regime. This means that the collision rate keeps increasing during the cooling. The change in collision rate can be obtained from a set of equations for the time evolution for the average density $\overline{n}$ and the average velocity $\overline{v}$ [20]:

$$\begin{aligned} \frac{d\overline{n}}{dt} &= A\overline{n}^2\overline{v} - (\tau\Gamma_{el})^{-1}\overline{n}, \\ \frac{d\overline{v}}{dt} &= -B\overline{n}\overline{v}^2, \end{aligned} \tag{1.7}$$

where A and B are constants depending on the frequency of the RF-field, τ is the trap lifetime and Γ_{el} is the initial collision rate. This set of equations can be solved for $\overline{nv}$, which will give the time evolution of the collision rate because that is given by $\overline{n\sigma v}$:

$$\overline{nv} = \frac{e^{-(\tau\Gamma_{el})^{-1}}}{1 - (1 - e^{-(\tau\Gamma_{el})^{-1}})\frac{A-B}{(\tau\Gamma_{el})^{-1}}}. \tag{1.8}$$

It can be seen from this solution that there are three types of behavior for $\frac{d}{dt}(\overline{nv})$, depending on the ratio of $A - B$ and $(\tau\Gamma_{el})^{-1}$. If $A - B < (\tau\Gamma_{el})^{-1}$ the collision rate is decreasing monotonously, if $A - B = (\tau\Gamma_{el})^{-1}$ it stays constant and if $A - B > (\tau\Gamma_{el})^{-1}$ then the collision rate keeps increasing. This is shown in Figure 1.4. It can be shown that $A - B$ never exceeds 0.0033 [20]. Now this places a lower limit on the initial collision rate times the trap lifetime. Runaway evaporative cooling occurs if the criterion:

$$\overline{n_0\sigma v_0} \cdot \tau > 300, \tag{1.9}$$

is fulfilled. Here $\overline{n_0 \sigma v_0}$ represents the average initial collision rate. In Appendix A a complete derivation of this criterion is given.

1.5 This Report

Improving the initial conditions for evaporative cooling and measuring the scattering length are the next steps that have to be taken in the process of creating a Ne* BEC. The improvement of the initial conditions, i.e. increasing the number of trapped atoms at a temperature as low as possible, is the subject of Chapter 2. Both changes to the vacuum and optical setup, aimed at improving the lifetime of the atoms in the MT and making the operation of the setup more stable, and experiments aimed at optimizing the transfer of atoms from the MOT to the MT are discussed. In Chapter 3 numerical simulations of a method to measure the scattering length, the two knives experiment, are discussed. Chapter 4 addresses the phenomenon of anharmonic mixing. This concerns the exchange of energy between the different dimensions of the magnetic trap and needs to be understood in order to be able to use the most promising method to measure the scattering length, the observation of collisional exchange of energy between those dimensions.

Chapter 2

Improving Initial Conditions for Evaporative Cooling

2.1 Introduction

Evaporative cooling can only succeed in reaching the BEC transition if the initial collision rate is high enough, as indicated by (1.9). That requires a large number of atoms and a low temperature in the magnetic trap because the collision rate depends on those parameters as $\overline{n\sigma v} \sim NT^{-2}$. In this Chapter two sets of experiments, spin polarization and optical molasses, are described that were aimed at improving those parameters. Furthermore, changes in the vacuum and optical setup are described that have lowered the background pressure in the trap chamber and have made the operation of the whole setup more stable and easier.

2.2 Setup

The setup consists of several different parts. The vacuum setup contains the source of metastable neon atoms, the part where the atomic beam is produced and the trap chamber, where the MOT and MT are situated and the experiments are done. There are two optical tables, one table where the laser, acousto-optical modulators (AOM's) and fiber incouplers are situated, and a table near the trap chamber containing only the fiber outcouplers and optics. Around the trap chamber there are three sets of coils to generate all the magnetic fields. One set is for the MT, one set for the MOT and there is one set of coils that is used to compensate stray magnetic fields. Furthermore the whole setup is computer-controlled. Detailed descriptions of the setup can be found in [21, 15, 22]. The vacuum setup and the optical setup have recently been changed significantly and will therefore be described in detail here.

2.2.1 Trap Chamber

The vacuum setup has two separate parts, the atomic beam and the trap chamber. The atomic beam part consists of a source, where a discharge produces metastable neon atoms, and several sections, denoted in Figure 2.3 as compressor, collimator, Zeeman slower and first and second cooler, where laser cooling is applied to increase the flux of atoms in the atomic beam up to approximately 10^{10}at/s. This part of the setup will not be discussed further here, it is extensively described in [15]. The pressure in the atomic beam part is on the order of 10^{-7}Torr. The trap chamber is connected to the atomic beam part by a differential pumping stage, which makes pressures below $6 \cdot 10^{-10}$Torr, the detection limit of the pressure gauge, possible in the trap chamber.

The lifetime of an atom cloud in the MT is determined mainly by the background pressure. Because the ion-getter pump that is connected to the trap chamber does not pump neon very well, a turbo-molecular pump had to be added to the trap chamber in order to reduce that background pressure. A test setup was built first to verify that the vacuum parts that were to be connected to the trap chamber could reach pressures below 10^{-9}Torr. In Figure 2.1 the test setup is shown. It was partially built inside a bake-out chamber. The bake-out chamber is an aluminum box which is equipped with four computer-controlled blow-driers. With this chamber it is possible to gradually raise the temperature to over 150°C without creating large temperature gradients. By heating up the test setup any dirt or deposit is removed from the inner surface of the vacuum parts. In order to be able to reach pressures below 10^{-9}Torr this is a necessary procedure. Creating temperature gradients has to be avoided as much as possible because these gradients can cause windows to fracture.

The ion-getter pump inside the bake-out chamber was used as a pressure meter, it can measure accurately down to 10^{-9}Torr. The second turbo-molecular pump and the pre-pump were used only to provide a backing vacuum of about 10^{-6}Torr for the turbo pump. When the turbo pump was connected to the trap chamber, the atomic beam part was used as the backing vacuum. The final pressure that was reached after the bake-out was below 10^{-9}Torr.

The trap chamber and the test setup were both filled with argon to avoid new deposit on the inner surfaces and were then connected. In Figure 2.2 the trap chamber is shown with the added turbo pump. The background pressure in the trap chamber is below $6 \cdot 10^{-10}$Torr when the vacuum valve between the trap chamber and the atomic beam part is closed and $3 \cdot 10^{-9}$Torr with the atomic beam operating. When compared to these pressures before the turbo pump was installed the pressure with the valve to the atomic beam part closed is about the same and with the atomic beam the pressure has now improved by a factor of two. The background pressure with the atomic beam operating is the most important figure, as this should determine the lifetime of an atom cloud in the MT. However, the measured improvement in this lifetime is much smaller, from 4s to 5s, suggesting that there may be another loss process that influences the lifetime.

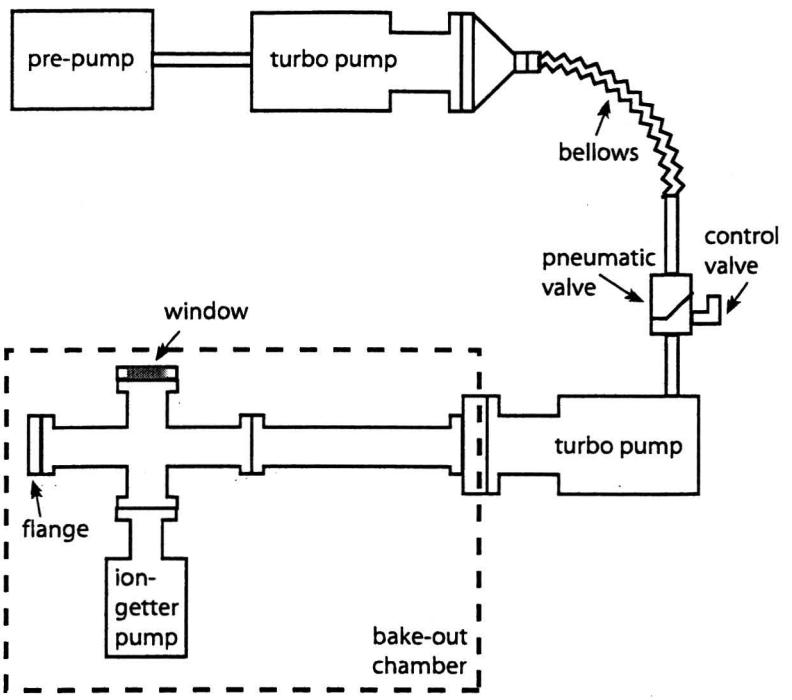

Figure 2.1: *Schematic drawing of the setup used to test the vacuum part with turbo pump that has been added to the trap chamber.*

2.2.2 Optical Setup

Neon has a closed optical transition from the $^3P_2$ to the $^3D_3$ state at a wavelength of 640.224nm. This transition is used for laser cooling, spin polarization of the atoms and absorption imaging. The optical setup has been modified in order to be able to generate the light needed for the atomic beam, the MOT and the spin polarization beam with a single dye laser. Before this modification a second dye laser was used for only the MOT beams, but because maintenance of the lasers requires up to 70% of the total maintenance time this was rather impractical.

The laser is locked to the atomic transition by passing it through an absorption cell. The laser detuning is controlled by a magnetic field in the cell and is set at -2Γ. This is the detuning at which the laser cooling sections of the atomic beam operate. Acousto-optical modulators (AOM's) are used to reach the right detuning for all other beams. An AOM is a crystal in which a radio-frequency standing wave is generated. A light beam is passed through the crystal perpendicular to the standing wave and is then Bragg-refracted by that standing wave. This slightly deflects the beam and changes its frequency by the frequency of the standing wave. Single mode polarization-preserving fibers are used to transport the light for the MOT and the spin polarization pulse from the optical table to the trap chamber. The optical setup is shown in Figure 2.3.

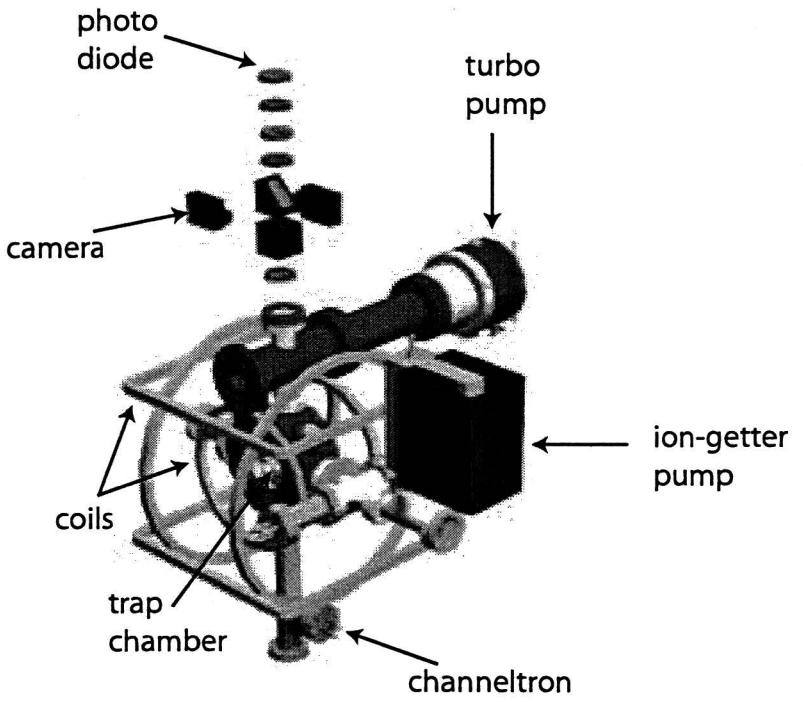

Figure 2.2: *Artist's impression of the trap chamber and surrounding parts of the setup.*

The MOT beam is passed through the same AOM, denoted by e in Figure 2.3, twice. This is done in order to be able to change the detuning of the beam without having to realign the incoupling in the fiber. This would otherwise be necessary because the deflection angle of the beam changes when the detuning is changed by the AOM. By sending it back along the same path with a lens and a mirror in the focal plane of the lens the change in deflection angle is cancelled while the change in detuning is doubled. In the AOM's from which both zeroth and first order are used, no light is lost. If only the first order is used, then the efficiencies are in the range $0.6 - 0.7$. This is the case for AOM's a,b,e and f in Figure 2.3.

The alignment of the laser itself is controlled by the two four-quadrant diodes. These diodes give the position of the laser beam on their surface, and by adjusting two mirrors that position can be kept constant.

The optical table near the trap chamber is shown in Figure 2.4. The upper fiber outcoupler is used for the light of the spin polarization pulse and the lower one for the MOT beam. The photo-diodes are used in a feedback loop in order to stabilize the intensity of the two light beams. The spin polarization pulse is also used for absorption imaging as described in the next Section, therefore it is reflected onto a digital camera.

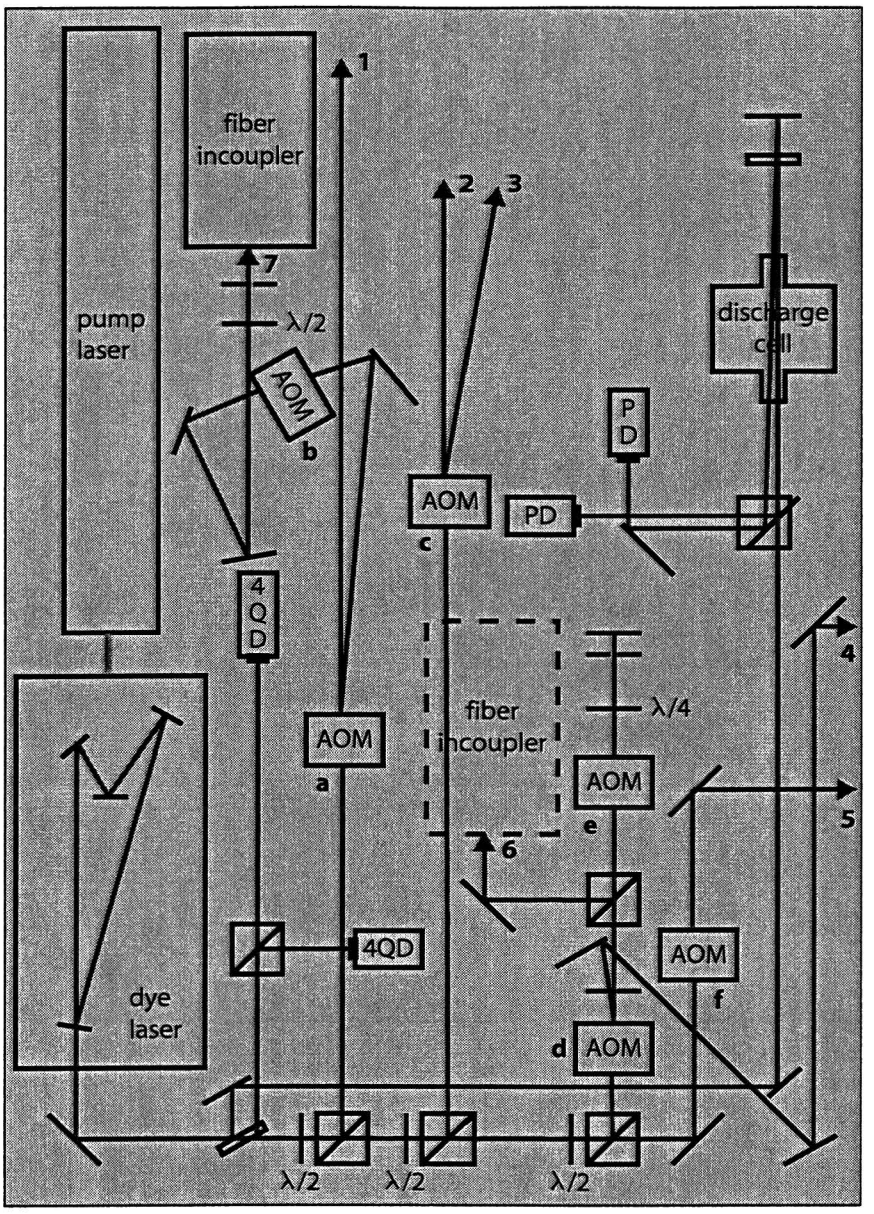

Figure 2.3: *Schematic outline of the optical setup. The numbers denote where the light is going to and with what power: 1=compressor (205mW), 2=Zeeman slower(100mW), 3=2nd cooler(95mW), 4=1st cooler(40mW), 5=collimator(80mW), 6=MOT beams (100mW), 7=spin polarization pulse. The intensities are based on a total power of 620mW coming out of the laser. The abbreviations mean the following: PD=photo diode, 4QD=four quadrant diode, AOM=acousto-optical modulator. The letters denote the AOM's, their frequencies are: a,b,e=40MHz, c=400MHz, d=70MHz and f=80MHz. The dashed line of the fiber incoupler indicates that it is elevated above the table.*

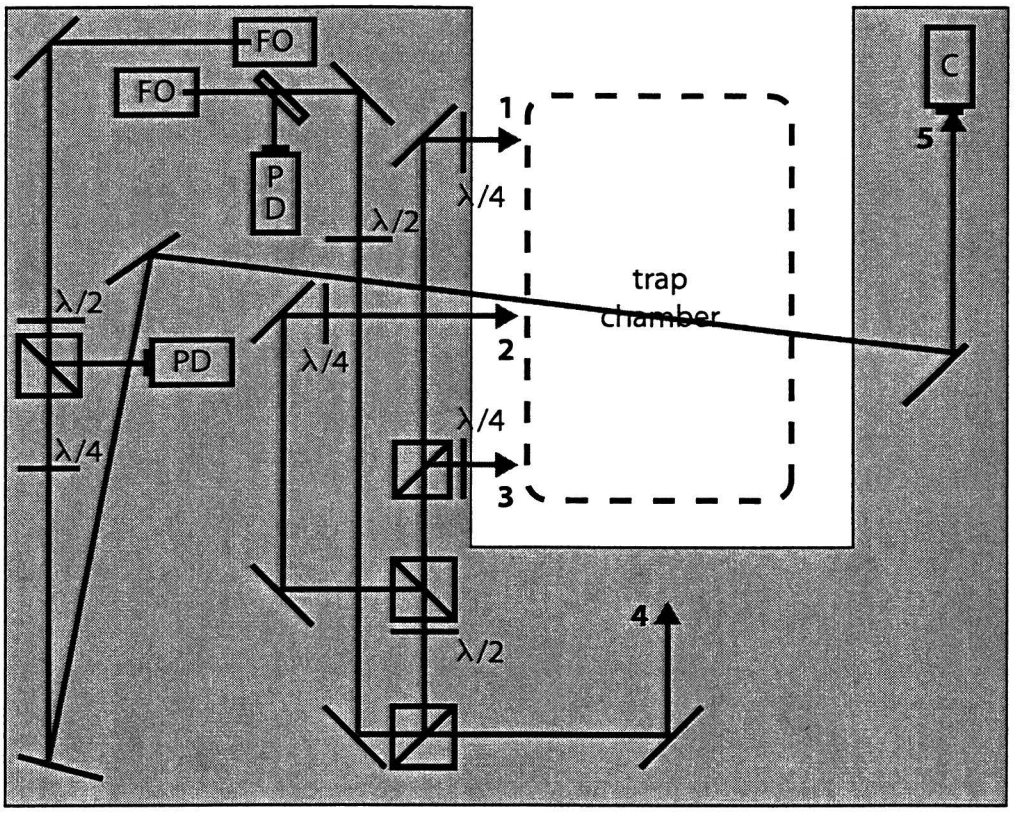

Figure 2.4: *Schematic outline of the optical setup near the trap chamber. The different light beams are denoted with numbers: 1,2,3=MOT beams, 4=second Zeeman slower and 5=spin polarization/absorption imaging pulse. The abbreviations mean the following: PD=photo diode, FO=fiber outcoupler and C=camera.*

2.2.3 Diagnostics

In order to be able to measure the number of atoms and temperature of the atom cloud, a number of diagnostics are available. Detecting the number of atoms can be done by recording the fluorescence intensity of the MOT. Fluorescence is the light that is spontaneously emitted by the atom cloud, its intensity is linear in the number of atoms. The fluorescence is focused onto a photo-diode by a lens that is placed on a window of the trap chamber, as shown in Figure 2.2. The number of atoms is given by:

$$N = P\frac{4\pi}{\Omega}\frac{1 + Cs + (2\delta/\Gamma)^2}{\hbar\omega C s\Gamma/2}, \tag{2.1}$$

where P is the fluorescence power, Ω the solid angle of the collecting lens and C the effective Clebsch-Gordan coefficient for all m_J states combined.

Both temperature and number of atoms can be determined with absorption imaging. An absorption image is taken by shooting an on-resonance pulse of 350μs duration through the atom cloud along the axial axis of the trap onto a CCD camera. The pulse that is also used for spin polarization, as shown in Figure 2.4 is used for this. The absorption profile is fitted with a two-dimensional gaussian, from which the rms diameters in the two radial directions are obtained. The average of those two values is taken as the radial diameter. When that diameter is measured as a function of the delay time between turning off the MOT or MT and the imaging pulse, the expansion velocity and thereby the temperature can be deduced. The temperature is determined by fitting the function:

$$\sigma(t) = \sqrt{\sigma_0^2 + \frac{k_B T}{m} t^2}, \tag{2.2}$$

where σ_0 is the initial radius and t the delay time, to the diameter. From the amount of absorption the number of atoms can be deduced.

Finally, temperature and number can be obtained from a channeltron measurement. The position of the channeltron is directly below the center of the trap, as shown in Figure 2.2. When the atoms are released from the trap, they fall down onto the channeltron. The channeltron consists of a grid of wires and a detector plate behind it. A large voltage difference of about 3kV is maintained between the grid and the detector, directed such that ions are repelled and electrons accelerated. The internal energy of the metastable atoms is released when the atoms hit the detector. The result is a voltage pulse proportional to the number of atoms that can be recorded. From the arrival time of the atoms at the detector the temperature can be deduced. With the channeltron it takes only a single measurement to obtain the temperature, contrary to absorption imaging where a series of images as a function of delay time is required.

2.3 Spin Polarization

2.3.1 Introduction

In the MOT up to 10^{10} atoms can be trapped, but different spin states are present. In the MT only the states $|m_J = +1\rangle$ and $|m_J = +2\rangle$ can be trapped, but trapping both states will result in large losses due to Penning ionization [22]:

$$\mathrm{Ne}^*(^3P_2) + \mathrm{Ne}^*(^3P_2) \rightarrow \mathrm{Ne}(^1S_0) + \mathrm{Ne}^+ + e^-. \tag{2.3}$$

This process can be suppressed by spin polarizing the atoms before transferring them into the MT. This is done by applying a σ^+ laser pulse, causing all atoms to be in the $|m_J = 2\rangle$ magnetic sub-state. An even more important consequence of spin polarizing the atoms is that all atoms in the MOT can be captured in the MT instead of only the ones that happen to be in the $|m_J = +1\rangle$ or $|m_J = +2\rangle$ states.

2.3.2 Analytical Model

The time evolution of the occupation of the different magnetic sub-states of the ground and excited state of the laser cooling transition under influence of a σ^+ light pulse can be described by rate equations. The processes that have to be described by these equations are absorption, stimulated emission and spontaneous emission. The rate of spontaneous emission is given by the linewidth Γ and the rates of absorption and stimulated emission, which are equal, by $j\sigma_{m_{J,g},m_{J,e}}$ where j is the photon flux and $\sigma_{m_{J,g},m_{J,e}}$ the absorption cross-section for a transition from ground state $|m_{J,g}\rangle$ to excited state $|m_{J,e}\rangle$. That cross-section depends on a number of parameters:

$$\sigma_{m_{J,g},m_{J,e}} = \frac{3}{4}\lambda^2 C_{CG}^2 \Gamma L(\delta(B),\Gamma), \tag{2.4}$$

where λ is the wavelength of the light, $L(\delta(B),\Gamma) = \frac{2}{\pi\Gamma(1+(2\delta/\Gamma)^2)}$ is the Lorentz profile of the absorption spectrum, in which the Zeeman shift of the different m_J states is accounted for in the detuning, and C_{CG} is the Clebsch-Gordan coefficient for the transition. The squared Clebsch-Gordan coefficient gives the rate for spontaneous emission from an excited to one of the ground sub-state relative to the total spontaneous emission rate.

Now a rate equation can be made for each of the magnetic sub-states, which symbolically looks like:

$$\frac{\partial n_{g,m_J}}{\partial t} \sim j\sigma_{m_{J,g},m_{J,e}}(n_{e,m_J+1} - n_{g,m_J}) + C_{CG}^2\Gamma n_e, \tag{2.5}$$

where n_{g,m_J} and n_{e,m_J} are the occupation numbers of the magnetic sub-states of the ground and excited states. The term $j\sigma n_e$ represents stimulated emission, $-j\sigma n_g$ represents absorption and $C_{CG}^2\Gamma n_e$ represents spontaneous emission. If only σ^+ light is present then the excited states with $m_J = -2, -3$ do not need to be considered, therefore a system of ten coupled differential equations such as (2.5), for five ground states and five excited states, will describe the time evolution of the occupation numbers. The full system of equations can be found in Appendix B.

The result of the numerical solution to these equations is shown in Figure 2.5. All atoms will end up in the $|m_J = 2\rangle$ state, the time it takes to get 95% in that state is 18μs with an on-resonance pulse and 6μs with a pulse that is detuned by 1.5Γ if the pulse intensity is 2mW/cm^2 and the magnetic bias field 4.3G. These are the parameters that are used in the experiments described in the next Section. The results of Figure 2.5 show that the Zeeman shift of the detuning is important, because without that shift the on-resonance pulse would transfer all the atoms to the $|m_J = 2\rangle$ state the fastest.

2.3.3 Experiments

The starting point for the experiments to optimize spin polarization is a MOT at a detuning of 2Γ to the red. The magnetic field, except for a bias field along the axial axis of 4.3G, and the light field of the MOT are turned off and at that moment a σ^+ light pulse is applied. The pulse is directed along the axial axis of the trap, at a small angle of about

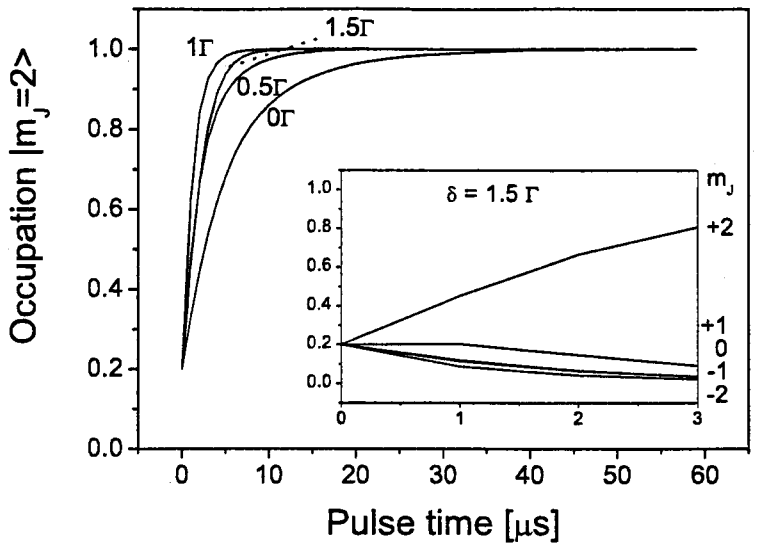

Figure 2.5: *Occupation of the* $|J = 2, m_J = 2\rangle$ *magnetic sub-state as a function of the length of the spin polarization. The four curves shown are for detunings of* $0, 0.5, 1.0$ *and* 1.5Γ. *At* $t = 0$ *the occupation of all sub-states is equal. In the inset the time evolution of the five magnetic sub-states is shown for a detuning of* 1.5Γ. *The intensity of the* σ^+*-pulse is* $2mW/cm^2$ *for all curves and the strength of the magnetic bias field is* $4.3G$.

5° because one of the MOT beams is directly on-axis. The pulse has to be directed this way because the alignment of the magnetic moment of the atoms should be along this axis in order to trap them in the MT. When the pulse has passed through the atom cloud the MT is turned on for 100ms. Now all the atoms still in the $m_J = -2, -1, 0$ states are lost while the $m_J = +1, +2$ states are trapped. After the MT is turned off again the atoms are recaptured in the MOT. Detecting the number of atoms before and after this process is done by recording the fluorescence intensity of the MOT. The efficiency of the spin polarization and subsequent transfer of atoms to the MT is determined by dividing the fluorescence intensities after and before the transfer.

The parameters that can be optimized are the length, polarization, intensity and detuning of the pulse. In Figure 2.6 the transfer efficiency is shown as a function of the pulse length. A weak maximum is observed at a pulse length of $50\mu s$, which is about twice the time that should have been needed according to the result of the model in Figure 2.5. The low transfer efficiency of about 30% at this pulse length is caused by the detuning of -0.2Γ, which is too far from the optimal value. The pulse should be kept as short as possible because then the increase in temperature is as small as possible. This increase is caused by the expansion of the atom cloud, which increases the added potential energy when the MT is turned on, and by spontaneous emission if more photons than necessary are scattered. In Section 2.4.2 the heating rate as a result of spontaneous emission is worked out. For

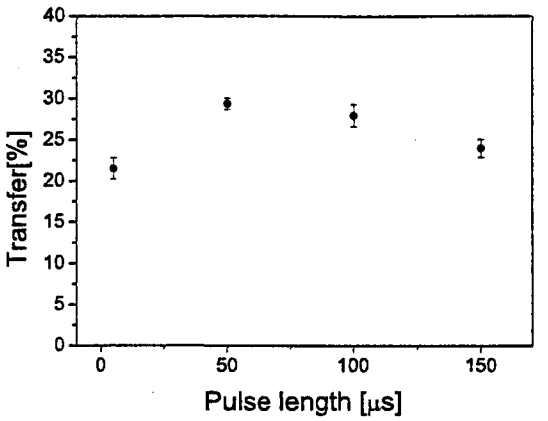

Figure 2.6: *Efficiency of the transfer of atoms from the MOT to the MT as a function of the length of the spin polarization pulse. The AOM control voltage is 5V and the pulse detuning is* -0.2Γ. *Three measurements were taken for each data point.*

the remaining experiments the pulse length is kept at $50\mu s$.

The light for the spin polarization pulse is taken from the compressor beam that is shown in Figure 2.3. The AOM placed in the beam is turned on. This changes the detuning of the beam by about 5Γ and also deflects it onto a mirror. It is then passed through a second AOM that shifts the detuning back by -5Γ and is coupled into an optical fiber that ends on the optical table near the trap chamber. The intensity of the pulse is determined by the power that is put into the first AOM. In Figure 2.7 the transfer efficiency is shown as a function of the control voltage of the AOM. The result resembles a step function, indicating that below 0.5V there is no pulse and below 1.0V the intensity is maximal. That intensity was measured to be 2mW/cm^2. For the rest of the experiments a control voltage of 3V was used.

The detuning of the pulse is controlled by the two AOM's described above. By changing the input frequency of these AOM's the detuning of the pulse is varied. Changing the input frequency of an AOM also changes the deflection angle of the light, therefore the incoupling into the fiber has to be redone. This makes the detuning the most impractical parameter to vary. The transfer efficiency as a function of detuning is shown in Figure 2.8. Measuring at a detuning higher than 1.5Γ was not possible because the range of frequencies of the two AOM's is limited. However, at a detuning of 1.5Γ the efficiency of spin polarization is already close to its maximum value.

2.3.4 Discussion

The experimentally found result for the optimal pulse length of about $50\mu s$ at a detuning of 1.5Γ is somewhat longer than the prediction of the model of Section 2.5. The difference

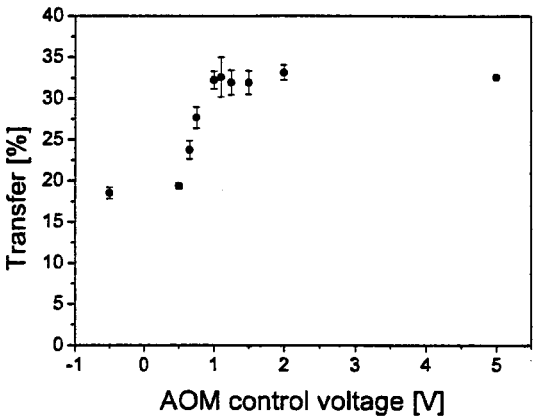

Figure 2.7: *Transfer efficiency as a function of the control voltage of the AOM that is used to switch the pulse. The pulse length is* $50\mu s$ *and the pulse detuning is* -0.2Γ. *Three measurements were taken for each data point.*

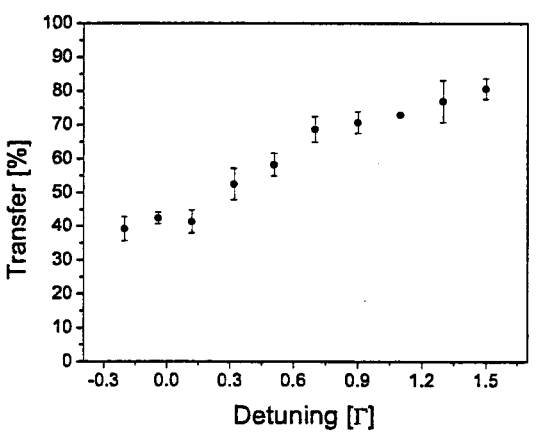

Figure 2.8: *Transfer efficiency as a function of the detuning of the spin polarization pulse. The pulse length is* $50\mu s$ *and the AOM control voltage is 3V. Three measurements were taken for each data point.*

is probably caused by imperfect circular polarization of the pulse. In the model the polarization is assumed to be perfect. In the experiment this is not the case, the quality of the polarization can be expressed as:

$$Q_{pol} = \frac{I_{max} - I_{min}}{I_{max} + I_{min}}, \tag{2.6}$$

where I_{max} and I_{min} are the maximum and minimum intensity of the pulse measured behind a polarizer that is rotated by 360°. A value of one indicates perfect linear polarization and zero indicates perfect circular polarization. In practice the optimal circular polarization yields a value of about 0.1.

The Zeeman shift is slightly different for different $m_{J,g} \rightarrow m_{J,e}$ transitions, but is on the order of 1Γ. The optimal detuning is therefore expected to be 1Γ, as was also found in Figure 2.5, but is experimentally found to be 1.5Γ. A reason might be a decrease in pulse intensity as a consequence of absorption of light. In the model the intensity is assumed to be constant, but in the experiment it decreases exponentially as a function of distance travelled through the atom cloud due to absorption, $I(z) = I_0 e^{-\sigma_{eg} n z}$. Further from resonance the effect of absorption is less important due the dependence of absorption cross-section (2.4) on the detuning.

The maximum transfer efficiency that was reached was 80%, as shown in Figure 2.8. This number is an underestimation of the real transfer however, due to a very fast decay of the MOT fluorescence after the recapture. This decay is caused by two-body losses, which are the dominant loss process at high densities and result in a much faster decrease of the density than would occur as a result of collisions with background gas atoms. Before the spin polarization the number of atoms in the MOT, and therefore the fluorescence intensity, is approximately constant because loss of atoms from the MOT is compensated by a capture of new atoms from the atomic beam. During the experiment the atomic beam is blocked and the number of atoms in the recaptured MOT decays as a result of two-body losses and collisions with background atoms. The fluorescence intensity is determined by averaging over a short time interval, so the atom loss during that interval causes the underestimation of the transfer efficiency. A realistic estimate of the real transfer efficiency is about 90%.

2.4 Optical Molasses

2.4.1 Introduction

The temperature of the atom cloud in the MT after the transfer from the MOT can be decreased by applying optical molasses before the spin polarization pulse. A lower temperature is desirable because then the initial conditions for evaporative cooling are better. Optical molasses consists of the application of three pairs of counter-propagating laser beams, for which the MOT beams are used. The cooling force is caused by the absorption of photons and subsequent spontaneous emission. Stimulated emission only comes into play

at high intensities, it is not considered in this Section and also does not contribute to the cooling force. When the beams are red detuned the beam that is propagating counter to the atom is Doppler shifted closer to resonance and the other beam away from resonance. Therefore red detuning gives a slowing force. This force is proportional to its velocity, $\vec{F} = -\beta\vec{v}$, over the relevant velocity range. After absorbing a photon the atom returns to the ground state by spontaneous emission. Spontaneous emission is responsible for heating of the atom cloud and therefore determines the lowest temperature that can be reached by applying optical molasses. This is the Doppler temperature, which is $T_D = 203\mu$K for Ne*.

2.4.2 Analytical Model

Just as the MOT described in Chapter 1, optical molasses depends on the absorption and re-emission of photons. These are processes which depend on probabilities, therefore the model described below gives an average effect on an atom; the final Doppler velocity is an average velocity, the energy distribution of the atom cloud remains thermal. Furthermore, stimulated emission is not taken into account here. Thus the model is only valid for $s_0 \ll 1$. The difference between the principle of a MOT and of molasses is that now the Doppler shift instead of the Zeeman shift is responsible for the difference in absorption from the beams propagating in opposite directions. The force that an atom experiences when molasses is applied is [16]:

$$\vec{F} = \frac{8\hbar k^2 \delta s_0 \vec{v}}{\Gamma(1 + s_0 + (2\delta/\Gamma)^2)^2}. \tag{2.7}$$

As can be seen from this expression, molasses only slows an atom if the detuning is negative and the maximal force is produced at a detuning of $\delta = -\Gamma/2$. The steady state temperature of the optical molasses is determined not only by (2.7), because that would yield $T = 0$, but also by a diffusion in momentum space as a result of spontaneous emission. The diffusion coefficient is given by:

$$D = 2(\Delta p)^2/(\Delta t) = 4\gamma_p(\hbar k)^2, \tag{2.8}$$

where $\gamma_p = \frac{s_0\Gamma/2}{1+s_0+(2\delta/\Gamma)^2}$ is the scattering rate. The steady state temperature is now given by $T = D/\beta k_B$ and at a detuning of $\delta = -\Gamma/2$ this results in the Doppler temperature $T_D = \hbar\Gamma/2k_B$.

Equation (2.7) shows that the application of optical molasses results in an exponential decrease of the temperature of the atom cloud with a time constant of $\tau = m/\beta$ towards the steady state temperature. When the saturation parameter is taken as $s_0 = 0.04$ and the detuning as $-\Gamma/2$, as in the experiments, the time it takes to cool an atom cloud from 1mK to 300μK is 94μs.

2.4.3 Experiments

The application of molasses should result in temperatures of the atom cloud close to the Doppler temperature. For the molasses experiments the MOT was operated at a detuning

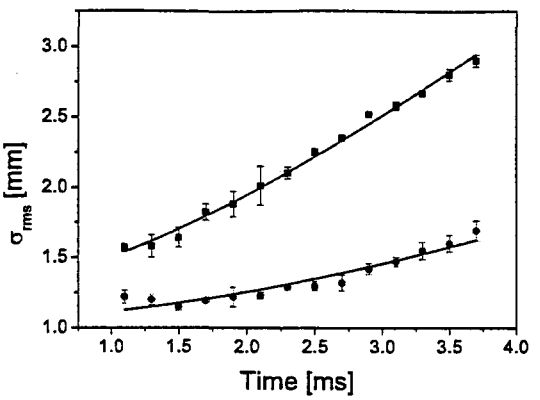

Figure 2.9: *Radial diameter of the atom cloud as a function of expansion time, determined by absorption imaging. For the square data points no molasses pulse was applied, the circular data points are with a* $500\mu s$ *molasses pulse. Four measurements were taken for each data point. The fits yield temperatures of* $300 \pm 60\mu K$ *and* $1.2 \pm 0.1mK$ *for the data with and without molasses pulse respectively.*

of approximately 2Γ in the red, where the number of trapped atoms was at a maximum. After turning off the MOT the molasses pulse was given. The length of the pulse was $500\mu s$ in this experiment and the intensity was 0.5mW/cm^2, corresponding to $s_0 = 0.04$. This was the highest intensity that could be used at that moment, with a higher intensity the same temperature would be reached in a shorter time. The temperature is determined by absorption imaging. Due to the large number of experiments that is needed to obtain the temperature of the cloud the pulse length has not been varied here. At every delay time the cloud diameter is measured with and without application of the molasses pulse. The result is shown in Figure 2.9, all data points are the average of four measurements. The data is fitted by (2.2), from which it is found that the molasses pulse has reduced the temperature from $1.2 \pm 0.1\text{mK}$ to $300 \pm 60\mu\text{K}$.

The goal of applying molasses is to reach temperatures as low as possible in the magnetic trap. Therefore the temperature is now determined when the atoms are spin polarized and transferred to the MT after the molasses pulse. The channeltron is used to measure the cloud temperature. With the channeltron it takes only a single measurement to obtain the temperature, therefore it was now possible to vary the molasses pulse length to find its optimal value. This was found to be $300\mu s$.

The intensity of the molasses pulse is again 0.5mW/cm^2 and the MOT is operated at 2Γ in the red. After the molasses pulse and the $50\mu s$ spin polarization pulse the atoms are held in the MT for 500ms. This is done to ensure that the atoms are in equilibrium in the MT and that the small fraction of atoms that was not captured in the MT has disappeared and does not fall onto the channeltron at the same time as the other atoms. When the MT is turned off again the atoms expand freely and a fraction hits the channeltron. In

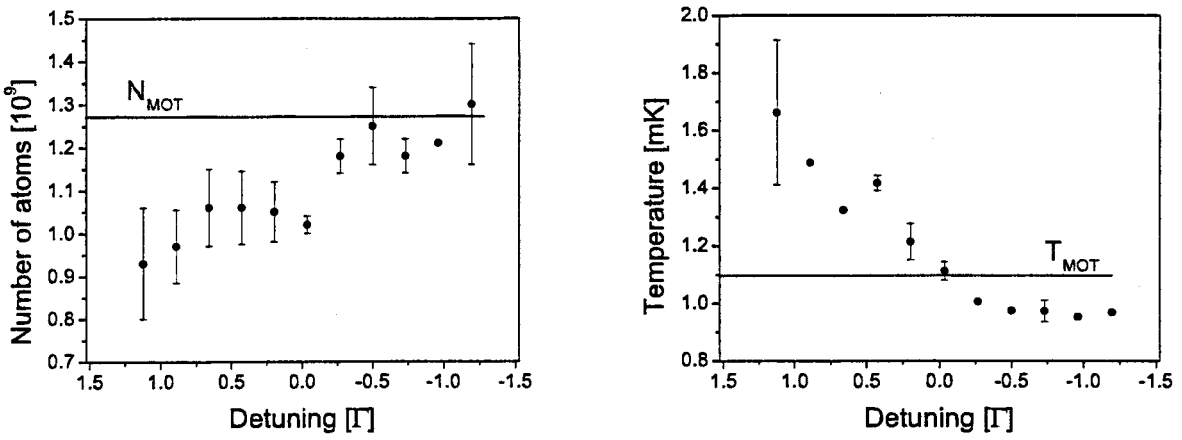

(a) (b)

Figure 2.10: *The lines in both graphs indicate the value without a molasses pulse. Two measurements were taken for each data point and the number of atoms and the temperature are determined by a channeltron measurement. a) Number of atoms as a function of the detuning of the molasses pulse. b) Temperature as a function of the detuning of the molasses pulse.*

Figure 2.10 the resulting temperature and number of atoms are shown as a function of the detuning of the molasses pulse. At blue detuning significant heating of the atom cloud and loss of atoms is observed. At a detuning of 0.5Γ to the red the atom loss is negligible and the temperature is reduced from 1.1mK to 0.95mK. This means that applying the molasses pulse has a positive effect on the initial conditions for evaporative cooling, but the temperature that is reached is still far from the Doppler temperature. Spin polarization and the transfer to the MT are responsible for increasing the temperature again after it has been lowered to about 300μK by the molasses pulse.

2.4.4 Discussion

The optimal pulse length for molasses was experimentally determined to be 300μs, longer than the predicted time of about 100μs. Factors that could have contributed to this result are a non-perfect polarization as described by (2.6) and a non-uniform intensity distribution over the three beams. The intensity for the three beams together of 0.5mW/cm^2 is distributed by two beam splitters. It was assumed that each beam then had an intensity of 0.17mW/cm^2, but if that was not the case then the time it takes to reach the final temperature would increase.

Another point is the optical density of the atom cloud. It is assumed that the intensity of the beams is constant over the whole cloud. If absorption becomes important, when the optical density of the cloud is not negligible, the intensity decreases from the side of the

cloud that is passed by the light beam first towards the other side. This means that except in the center the intensities of the two counterpropagating beams are not equal. This might also explain the dip in Figure 2.9 at 1.5ms. Due to an unequal intensity distribution the atoms could gain a drift velocity towards the center of the cloud, so the pulse compresses the cloud.

The effect of molasses after the transfer to the MT is very small. The temperature of 300μK after molasses is increased again to 950μK. The main cause for this is probably a mismatch of the centers and the sizes of the MOT and MT. If the centers of the MOT and MT do not overlap exactly, extra potential energy is added to the atom cloud when the MT is turned on. Even if the centers overlap, extra potential energy can be added because the diameter of the cloud is too large compared to its equilibrium value in the MT at the cloud temperature. This potential energy is converted to kinetic energy during the 500ms that the cloud is held in the MT, so that it is a lot hotter when the MT is turned off again. The expansion of the cloud during molasses and spin polarization does not play a large role, because the time between turning off the MOT and turning on the MT is on the order of 500μs, which is very short compared to the time it takes the cloud to expand significantly. This can be concluded from Figure 2.9, where the diameter does not increase significantly during the first two ms of the time-of-flight measurement.

In order to reach lower temperatures in the MT more work is needed on the exact matching of the size and position of the MT to the cloud. The diameter of the MT can not be increased further, but it is possible to compress the cloud before applying the molasses by shifting the detuning of the MOT closer to resonance just before turning it off. Exact matching is very hard to accomplish, therefore a more promising approach is to apply optical molasses in the MT. That way no matching is required anymore.

Chapter 3

Two Knives Experiment

3.1 Introduction

The two knives experiment is a technique to measure the scattering length developed by Browaeys *et.al.* [23]. Their reason for using this technique instead of the one described in Chapter 4 is that absorption imaging of their helium atoms was difficult due to lack of a good CCD camera at 1083nm. Since the scattering length is one of the key parameters determining the efficiency of evaporative cooling, it is important to be able to measure its value. The most common technique to measure the scattering length is based on observing the rate of relaxation of an atom cloud in a magnetic trap through elastic collisions towards equilibrium after it has been put in a non-equilibrium state. The two knives technique is based on the same principle.

By applying a RF knife and ramp the applied frequency down all atoms with an energy above the truncation energy $\varepsilon_t = \hbar\omega_{RF,end}$ are removed and the thermal energy distribution is cut off. Through elastic collisions the cloud will restore thermal equilibrium, thereby refilling the high-energy tail of the Boltzmann energy distribution. By waiting for a certain time, applying the same RF ramp again and measuring the number of atoms that have reentered the tail of the Boltzmann distribution the scattering length can be determined. A graphical representation of the two knives technique is shown in Figure 3.1.

The advantage of the two knives technique is that, assuming a three-dimensional cut, only the total energy of each atom is important. This means that anharmonic mixing, discussed in Chapter 4, does not disturb an experiment. The drawback of the two knives technique is that the refilling of the tail can also occur if there is a heating mechanism in place in the experiment. Collisions with background gas atoms and inelastic two-body collisions can cause heating, but also external causes like noise on the current through the coils of the magnetic trap or insufficient shielding of light at the transition wavelength may heat up the cloud. Separate measurement of the heating rate in the atomic sample is therefore required.

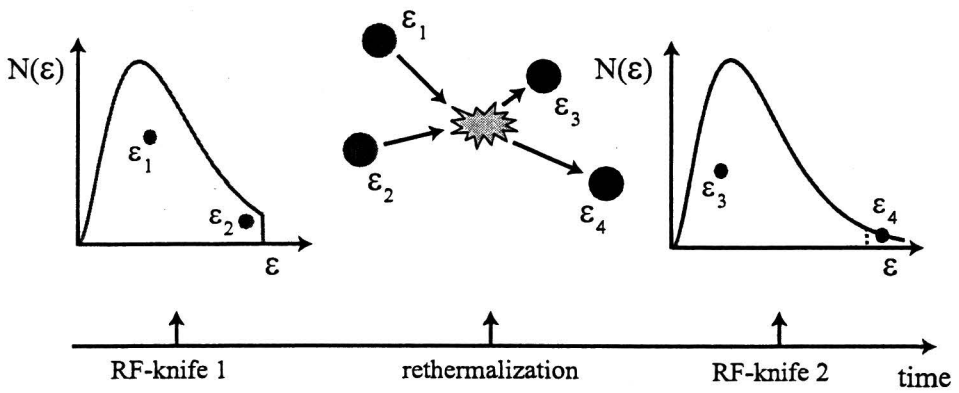

Figure 3.1: *Artists impression of the two knives technique. Shown are the cut-off energy distribution $N(\varepsilon)$ after application of the first RF knife, the process of rethermalization by atomic collisions between the two knives and a rethermalized energy distribution at the moment when the second knife is applied.*

3.2 Theory

3.2.1 Ergodicity

Ergodicity is a concept relating to the dynamics of a system. A number of different definitions of ergodicity can be given, depending on the exact application. The general idea is well represented by the following statement: "When a system is said to be ergodic it means that given enough time the system will sample all states available to it with equal probability". For an atom in a trap this means that its trajectory in phase space should fill a complete energy surface, not just a part of it. Defining ergodicity like this assumes that the system can take an infinitely long time in order to fulfill this demand. What is important from a practical point of view is if the system is able to reach any point on the available energy surface on a timescale short compared to other timescales relevant to the system. When this criterion is met the system is called "sufficiently ergodic".

Ergodicity of a system is a property that is very hard to prove, but it is believed that all many-body systems in nature are ergodic [24]. The reason for this is that interactions between atoms disturb any non-ergodic behavior. Sufficient ergodicity is therefore a justifiable assumption for properties of an atom cloud in a trap that vary on a timescale longer than a few collision times. This leaves open what happens on shorter timescales. This is particularly important in relation to evaporative cooling, where it is usually assumed that an atom with an energy above ε_t is removed from the trap before it can collide again. If the mechanism responsible for removing the atom depends on the energy of the atom in a particular direction instead of its total energy, such as when gravitational sag occurs [25] or when there is a contact surface [26], the assumption of sufficient ergodicity loses its validity. This changes the dimensionality of the evaporative cooling from three- to two- or

one-dimensional, thereby reducing the efficiency of the cooling process dramatically.

3.2.2 Kinetic Equation

The trapped atom cloud can be described as an ideal classical gas. This description can be applied to evaporative cooling as well as to the two knives experiment. The evolution of the phase space distribution function $f(\mathbf{r},\mathbf{p})$ of a classical gas is described by the Boltzmann equation [27]:

$$(\frac{\mathbf{p}}{m} \cdot \nabla_{\mathbf{r}} - \nabla_{\mathbf{r}} U \cdot \nabla_{\mathbf{p}} + \frac{\partial}{\partial t}) f(\mathbf{r},\mathbf{p}) = C(\mathbf{r},\mathbf{p}), \tag{3.1}$$

where $C(\mathbf{r},\mathbf{p})$ is the elastic collision integral. The elastic collision integral represents the effect that elastic collisions have on the distribution function. A detailed derivation of this integral is given in [28].

The assumption of sufficient ergodicity as discussed in the previous section has as a consequence that the phase space distribution function contains the same information as the energy distribution function combined with the density of states of the trap $\rho(\varepsilon)$. Therefore the Boltzmann equation can be simplified to an equation describing the time evolution of the energy distribution function $f(\varepsilon)$ instead of $f(\mathbf{r},\mathbf{p})$ by applying the operator:

$$(2\pi\hbar)^{-3} \int d^3r d^3p \delta(U(\mathbf{r}) + \frac{\mathbf{p}^2}{2m} - \varepsilon) \tag{3.2}$$

to both sides of (3.1). What happens by applying this operator is essentially a projection of the six-dimensional phase space onto the (one-dimensional) energy space. The gradient terms in 3.1 cancel each other when (3.2) is applied and what remains is a kinetic equation for $\frac{\partial}{\partial t} f(\varepsilon)$:

$$\rho(\varepsilon_4)\dot{f}(\varepsilon_4) = \frac{m\sigma}{\pi^2\hbar^3} \int\int\int d\varepsilon_1 d\varepsilon_2 d\varepsilon_3 \delta(\varepsilon_1+\varepsilon_2-\varepsilon_3-\varepsilon_4)\rho(min[\varepsilon_1,\varepsilon_2,\varepsilon_3,\varepsilon_4])\{f(\varepsilon_1)f(\varepsilon_2)-f(\varepsilon_3)f(\varepsilon_4)\}, \tag{3.3}$$

where the energies ε_i are as shown in Figure 3.1. Here the term $f(\varepsilon_1)f(\varepsilon_2)$ represents collisions between atoms with respective energies ε_1 and ε_2 resulting in an increase in atoms with energy ε_4, and the term $f(\varepsilon_3)f(\varepsilon_4)$ represents collisions that result in a decrease in atoms with energy ε_4.

It is assumed here that all particles can collide with each other. If collisions are needed for sufficient ergodicity, this assumption is formally not valid. An atom then only 'sees' a small fraction of the total number of atoms. The energy distribution of that fraction will also be thermal however, so Equation (3.3) will yield the correct result even in the case where collisions are needed for sufficient ergodicity.

3.2.3 Analytical Model

A simple analytical model is used by Browaeys *et.al.* that describes the refilling of the tail of the distribution function after the tail has been emptied [23]. The model is based on

the Boltzmann equation and sufficient ergodicity is again assumed. A distinction is made between the number of atoms N_- that have an energy ε_- lower than the truncation energy $\varepsilon_t = \eta k_B T$ and the number of atoms N_+ with an energy ε_+ higher than the truncation energy. At $t = 0$ the RF knife is applied, therefore $N_+(0) = 0$ and $N_-(0) = qN_{tot}(0)$ with q denoting the fraction of atoms that is below the truncation energy at $t = 0$. Now a rate equation can be formulated for the change in N_+:

$$\frac{\partial N_+}{\partial t} = \Delta_1 N_-^2 - \Delta_2 N_- N_+, \tag{3.4}$$

where Δ_1 and Δ_2 are coefficients that can be calculated from equation (3.3). In this equation collisions between atoms that both have an energy higher than $\eta k_B T$ are neglected because it is assumed that $\eta \gg 1$ and therefore the contribution from N_+^2 is very small. Furthermore it is helpful to realize that the term $\Delta_1 N_-^2$ is equal to the atom loss in the evaporative cooling process as described in [28]. In order to be able to evaluate Δ_1 and Δ_2 the assumption is made that the distributions in ε_- and ε_+ are thermal. Due to the limited number of atoms that leave ε_- and the thermal nature of the distribution at $t = 0$ this assumption is justified for the atoms in ε_-, but for the atoms in ε_+ it is questionable on timescales small compared to the scattering time.

According to Snoke and Wolfe [29] the distribution restores thermal equilibrium in typically four scattering times, so then the assumption is valid again. However, the results obtained by Luiten *et.al.* [27] and the results presented in this Chapter indicate that this may take considerably longer. Another assumption that is, implicitly, made in this model is that the temperature of the cloud does not change. It is shown in Section 3.4.2 that this assumption is incorrect. As a result of a decrease in temperature the number of atoms in ε_+ is overestimated by the model.

With those assumptions it is now possible to find the solution of (3.4), that is given by:

$$\begin{aligned} N_+(t) &= (1-q)N_-(0)e^{-t/\tau}[1 + \frac{q}{1-q-exp[(\tau/\tau_{th})(1-e^{-t/\tau})]}], \\ \tau_{th}^{-1} &= (\gamma_{el}/\sqrt{2})\frac{q}{1-q}e^{-\eta V_{ev}/V_e}, \end{aligned} \tag{3.5}$$

where τ is the lifetime of the atom cloud due to background collisions and the decay of the metastable state, τ_{th} is the rethermalization time, $\gamma_{el} = n\sigma\overline{v}$ the elastic collision rate and V_{ev} and V_e two reference volumes as defined in [27]. The product $\tau_{th}\gamma_{el}$ denotes the number of collisions that is needed for the rethermalization of the atom cloud. In [23] the solution of the second equation of (3.5) is compared to a numerical simulation of the Boltzmann equation, for which no assumption about the shape of the distribution function had to be made. There it was found that the model yields good results only for $\eta > 10$, for $\eta = 6$ the value of $\tau_{th}\gamma_{el}$ that is obtained from the model is 1.8 times too small.

3.3 Simulation

For the model of the previous Section, some assumptions were made that are not fully justified. These assumptions do not have to be made if equation (3.3) is solved numerically. Furthermore, a thermodynamic treatment such as in [27] or in Appendix A can not be applied when the number of atoms above ε_t is to be determined because those treatments specifically assume thermal equilibrium, which is not case if atoms are present above ε_t.

In order to be able to solve equation (3.3) numerically the energy is now discretized. The range of energies the atoms are confined to, that is from $\varepsilon = 0$ up to the trap depth U_{max}, are divided into n energy bins with width $\Delta\varepsilon = U_{max}/n$ and energy $\varepsilon_i = (i-1/2)\Delta\varepsilon$, $(i = 1..n)$. The trap depth is taken to be 12mK, because that is the experimental value. Discretizing (3.3) yields:

$$\rho_i \dot{f}_i = \frac{m\sigma}{\pi^2\hbar^3}(\Delta\varepsilon)^2 \sum_{k=0}^{n}\sum_{l=k}^{n} \rho(min[k,l,i,j])\{f_k f_l - f_i f_j\}, \tag{3.6}$$

where $j = k + l - i$. This equation is integrated by an Euler method. The number of bins is 64 when the initial temperature of the atom cloud is 1mK and is inversely proportional to that temperature. It has been checked that with 32 bins the same results are obtained. This ensures that the number of bins is always enough to be able to discretize the distribution function correctly. An advantage of calculating the distribution function is that no assumption has to be made about the nature of that distribution. This is contrary to the most common approach of modelling evaporative cooling, where the distribution function is assumed to be a truncated Boltzmann distribution and a thermodynamic treatment of the evaporation process is used [27, 28]. With the method used here it can be demonstrated that that assumption is valid however.

There are a number of parameters that are needed to accurately describe the behavior of a cloud of atoms in the two knives experiment. The magnetic trap that is used here is a Ioffe-Quadrupole trap, as described extensively in Chapter 4. It can be characterized by a bias field, field gradient and field curvature. The initial state of the atom cloud can be characterized by the temperature, a parameter η denoting the truncation energy $\eta k_B T$ and the number of atoms. Furthermore, in all the simulations the scattering length is taken to be $50a_0$, with a_0 the Bohr radius. Because the time it takes a cloud to rethermalize and to refill the tail of the Boltzmann distribution is determined by the collision rate, that time scales with the scattering length squared.

3.4 Results

3.4.1 Rethermalization

In order to verify if rethermalization always occurs, and therefore if the program functions correctly, the evolution of the distribution function is simulated starting with constant $f(\varepsilon)$.

Number of atoms	N	$1 \cdot 10^7$
Temperature	T	1mK
Magnetic bias field	B_0	1G
Magnetic field gradient	α	$1 \cdot 10^4 \mathrm{G/m}$
Magnetic field curvature	β	$47.5 \cdot 10^4 \mathrm{G/m^2}$
Truncation energy	η	6
Scattering length	a	$50a_0$

Table 3.1: *Default values of parameters used in the simulation.*

This situation can be thought of as 'infinite' temperature, and is nowhere near equilibrium. If the desired physical behavior is obtained, i.e. if the distribution moves towards thermal equilibrium, then it can be assumed that this also happens for a truncated distribution at a finite temperature. The RF knife is kept on the entire time, therefore the atoms that gain an energy higher than the truncation energy after a collision are instantly removed. The results shown in Figure 3.2 are the distributions of atoms as a function of energy, which are obtained by multiplying the distribution functions with the density of states (4.5). The distributions are labelled by the number of collisions per atom. Except at temperatures so low that quantum effects start playing a role [29], it takes a certain number of collisions per atom to rethermalize. A high initial collision rate is therefore important for fast rethermalization. In Figure 3.2, the evolution towards the familiar Maxwell-Boltzmann shape of the atom distribution can be observed clearly. This result can be compared with a result obtained by Luiten *et.al.* [27], where the result of a simulation with the same initial distribution is shown. Because the results obtained are comparable the conclusion can be drawn that the program yields the desired physical behavior and functions correctly.

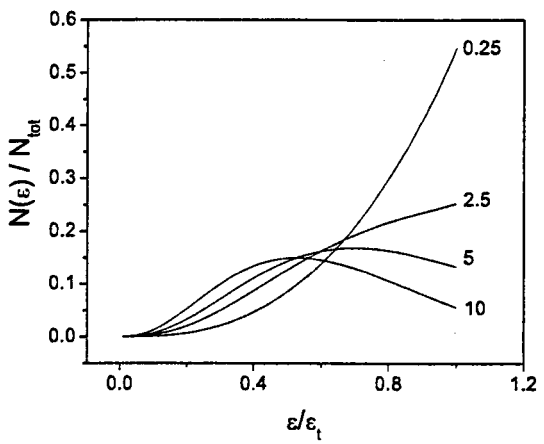

Figure 3.2: *Distribution of atoms as a function of energy. The energy is scaled by the truncation energy ε_t. The different curves are labelled by the number of collisions per atom.*

It is important to realize that there is a difference between thermalization of a cloud that has a cut-off energy distribution and thermalization of a cloud that is characterized by two different temperatures, a case that is discussed in Chapter 4. For the latter it is known from Monte-Carlo simulations that it takes approximately 2.7 collisions to rethermalize the cloud [30, 31].

3.4.2 Tail Refilling

The RF knife will now be turned off after it has removed all the atoms above the truncation energy. What is important for the two knives experiment is the refilling of the truncated tail of the distribution. When the second RF knife is applied the absolute number of atoms that is removed by that knife can be measured by for instance a channeltron. From that number and the rethermalization time between the two knives a value for the scattering length can be obtained. The exact shape of the energy distribution above ε_t can in principle also be measured with a channeltron, but is not needed for the determination of the scattering length.

In Figure 3.3 the energy distribution of the whole atom cloud is shown at different times. In the inset the refilling of the tail can be seen in detail. The discontinuity at $\varepsilon = \varepsilon_t$ has disappeared after approximately eight collision times, but it can be seen that after four collision times the distribution is still far away from its equilibrium state, contrary to the results in [29].

The effect of the evolution of the tail of the energy distribution can be expressed more quantitatively in number of atoms in the tail and temperature of the distribution below ε_t. In Figure 3.4 the time evolution of these quantities is shown. Taking the finite lifetime of the atomic sample into account influences the results for the absolute number of atoms the most. The number of collisions after which the number of atoms in the tail is at a maximum is now depending on the lifetime, because at that point the loss rate due to the metastable decay (or collisions with background gas atoms) overtakes the rate at which collisions refill the tail. The number of atoms in the tail does not exceed 50% of the number of atoms that was cut off by the first RF-knife. From the number of atoms in the trap relative to the number there would be in thermal equilibrium it can be concluded that it takes over 20 collisions to fully rethermalize the whole distribution.

The temperature evolution that is shown in Figure 3.4(c) has been determined by fitting a Boltzmann distribution to the calculated distribution below ε_t. For short times, i.e. when the number of atoms in the tail is still negligible, this evolution represents the effect of evaporative cooling. When the tail refills the rate of decrease of the temperature becomes smaller than it would be in the evaporative cooling process because collisions between atoms above and below ε_t slow down the process and because the truncation parameter is increasing. After 20 collisions the temperature has dropped by approximately 15%, which has changed the truncation parameter η from 6 to 7. This causes a decrease in the number of atoms above ε_t in thermal equilibrium by about 40%. This is not taken into account in the model of Section 3.2.3.

When doing the experiment it is necessary to measure the number of atoms in the

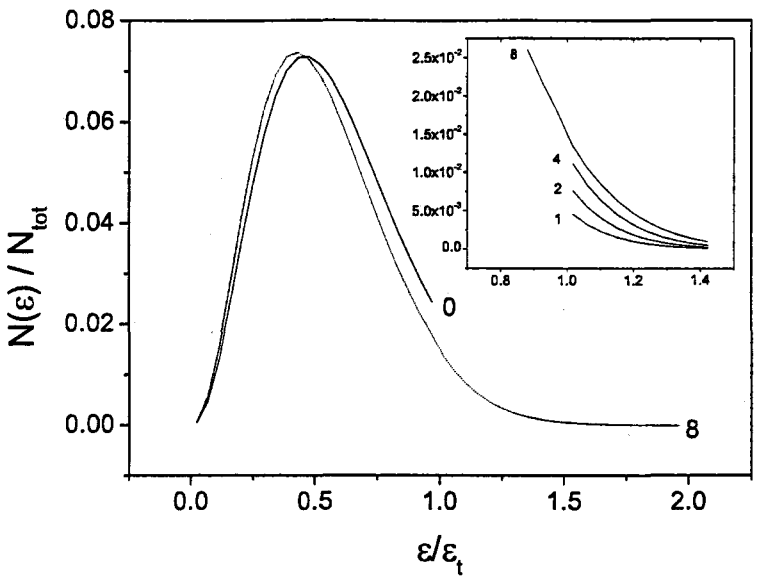

Figure 3.3: *The distribution function is shown right after the truncation and after eight collision times, when the discontinuity at $\varepsilon = \varepsilon_t$ has disappeared. In the inset the tail refilling is shown in more detail. The curves are labelled by the number of collisions per atom.*

tail as a function of the time between the two knives. By comparing the result obtained that way with the results for the absolute number of atoms from simulations at different scattering lengths it is possible to determine the correct value for the scattering length.

3.4.3 Experiment

The two knives technique has been applied experimentally two years ago by Claessens *et.al.* [28]. In Figure 3.5 a measurement is shown in which the end frequency of the RF knives is 120Mhz, corresponding to a value for the truncation parameter η of approximately 4.5. The temperature of the atom cloud is approximately 1.1mK. The fraction of atoms that is removed by the first RF knife is indicated by the dashed line in the figure. That value is measured separately when a two knives experiment is performed. From measurements such as the one shown in Figure 3.5 and the analytical model of Section 3.2.3 a value for the scattering length can be obtained. However, the range of values that were obtained is as large as $0 - 300a_0$ [28]. Not taking the change in temperature into account in the model clearly gives flawed results.

When the change in temperature is taken into account when analyzing the data in Figure 3.5, it becomes clear that the refilling of the tail is due to heating. In the previous Section it was shown that the fraction in the refilled tail could not exceed 50% of its value before the truncation if $\eta = 6$. In this experiment $\eta = 4.5$, therefore the cooling

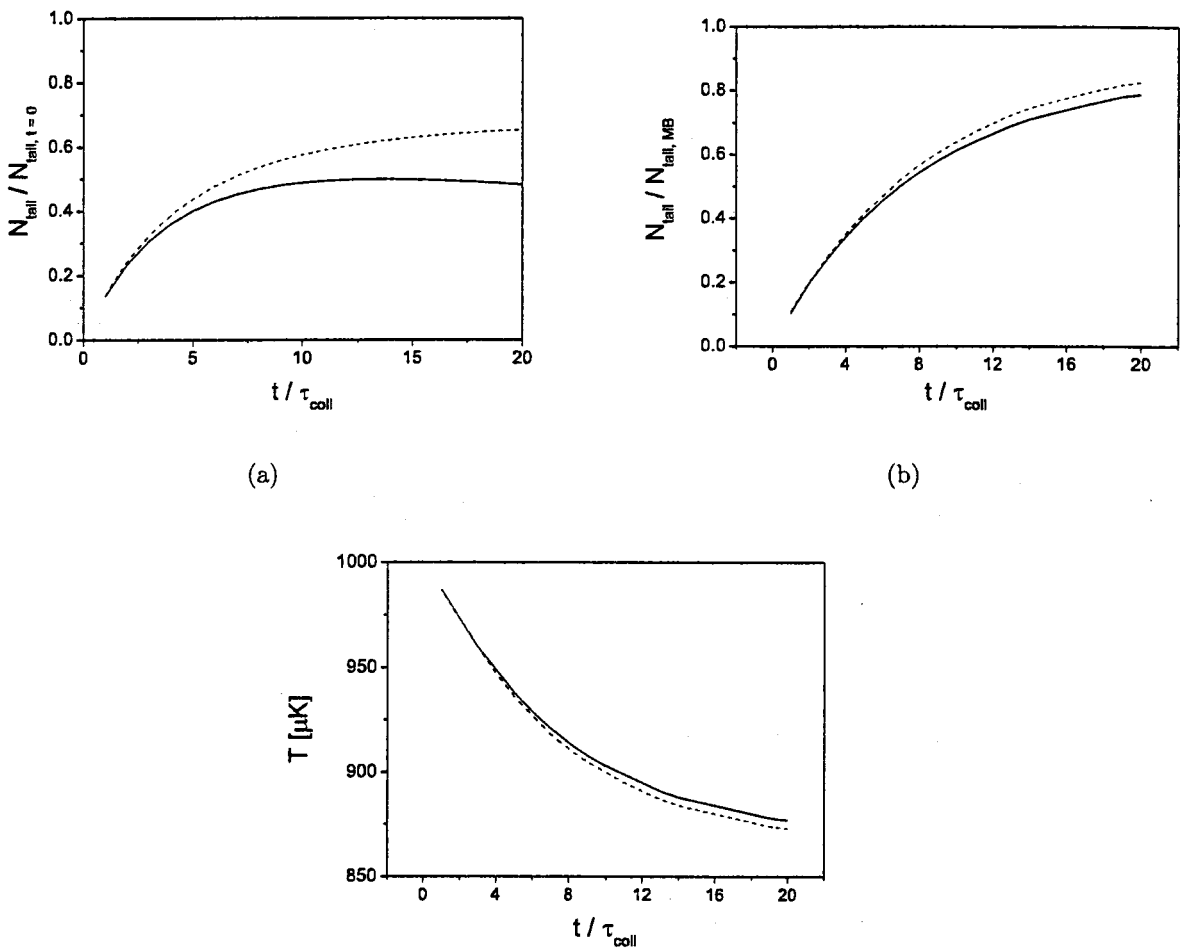

Figure 3.4: *The solid curves represent functions in which the lifetime of the metastable state is included, in the dashed curves there is no decay. a) The total number of atoms above ε_t, divided by its value before the first RF-knife is applied, as a function of time. b) The number of atoms above ε_t divided by the number of atoms there would be in a Maxwell-Boltzmann distribution of the same temperature as a function of time. c) The temperature of the atom cloud as a function of time.*

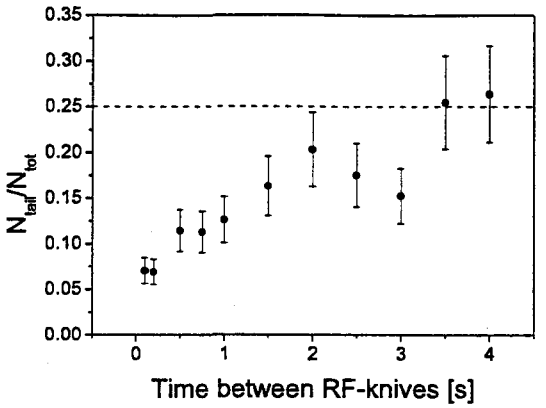

Figure 3.5: *The fraction of atoms that is removed by the second RF knife is shown as a function of time. The dashed line shows the number of atoms removed by the first RF knife.*

should be even larger and the fraction in the completely refilled tail should be smaller than $N_{tail}/N_{tot} = 50\% \cdot N_{tail,t=0} = 0.5 \cdot 0.25 = 0.125$. Because the fraction in the tail becomes much larger than that, it is clear that the refilling is caused by heating. No value for the scattering length can therefore be obtained from this experiment with the method described in this Chapter.

The heating rate has been measured to be as large as 80μK/s [28]. The heating is caused mainly by stray light entering the trap chamber and collisions of the trapped atoms with the background gas. Better shielding of stray light and a much lower background pressure are needed in order to be able to determine the scattering length this way.

Chapter 4

Anharmonic Mixing

4.1 Introduction

For trapped atoms, an important parameter is the ratio of the mean free path $\lambda = \frac{1}{n\sigma v}$, where n is the average density, σ the collision cross-section and v the average atomic velocity, and the characteristic size of the trap D. If the trapped atomic cloud is in the Knudsen regime, $\lambda \gg D$, the dynamics of collisionless motion can become important. For instance the validity of the assumption of sufficient ergodicity, as discussed in Chapter 3, depends on that dynamics. Also, the dimensionality of evaporative cooling is determined by it in the case where gravitational sag plays a role in the trap geometry or where an absorbing wall is used instead of an RF-field to remove atoms [32]. Almost all existing atom traps are in the Knudsen regime, indicating the importance of the understanding of collisionless dynamics. In order to investigate the influence of collisionless motion on the behavior of an atom cloud in a magnetic trap, the time evolution of a cloud of non-interacting atoms is simulated in this Chapter.

The magnetic trap is a Ioffe Quadrupole trap, which consists of three pairs of coils. The bias coils produce a homogeneous bias field B_0 in the axial direction. The pinch coils produce a harmonic trapping field in the axial direction with curvature β and the gradient coils produce a quadrupole field in the radial direction, which has a gradient α near the trap center. The trap geometry is described extensively in [21].

4.2 Theory

4.2.1 Magnetic Potential

The potential of a Ioffe quadrupole trap can be described by [33]

$$\begin{aligned} U(x,y,z) =& \mu[B_0^2 + (\alpha^2 - B_0\beta)(x^2+y^2) + 2B_0\beta z^2 + \frac{1}{4}\beta^2(x^2+y^2)^2 + \beta^2 z^4 + \\ & 2\alpha\beta(x^2-y^2)z]^{1/2} - \mu B_0, \end{aligned} \tag{4.1}$$

where μ is the magnetic moment of the atom, which is $3\mu_B$ for $^{20}Ne^*$ with μ_B the Bohr magneton. Terms that are higher than fourth order are neglected in this expression. The $(x^2-y^2)z$-term in (4.1) couples the motion in the axial (z) and radial (x and y) directions, therefore it is responsible for the transfer of energy between these directions. The strength of the coupling depends mainly on the magnitude of this term compared with the dominant second-order terms in (4.1). The x- and y-directions are always coupled much stronger than the axial and radial directions because they have the same trap frequency. This makes the coupling resonant, as is described in Section 4.5.

In the limit where the energy of the atom is much smaller than the potential energy at the trap center, $3k_bT \ll \mu B_0$, expression (4.1) reduces to the harmonic potential

$$U(r,z) = \frac{m}{2}(\omega_r^2 r^2 + \omega_z^2 z^2), \tag{4.2}$$

where m is the atomic mass, $r = (x^2+y^2)^{1/2}$ the radial coordinate, $\omega_r = [\frac{\mu}{m}(\alpha^2/B_0 - \beta)]^{1/2}$ the radial trap frequency, and $\omega_z = (\mu\beta/m)^{1/2}$ the axial trap frequency. In this limit there is no coupling between axial and radial motion.

Expression (4.1) represents the real potential only close to the trap center. Due to the finite dimensions of the coils that generate the magnetic fields, saddle points occur at some distance from the center. At these points the force on the atoms is directed away from the trap center and the atoms can therefore not be trapped anymore beyond those points. Trapping near the center can occur only if $\frac{B_0\beta}{\alpha^2} < 1$ and if the energy of the atom is small enough [34]. The potential has additional fixed points inside the region where trapping is possible that determine the character of the motion [33]. Four elliptic points are located at

$$(x,y,z) = (0, \pm\frac{\alpha}{\beta}\sqrt{2(\frac{B_0\beta}{\alpha^2}+1)}, \frac{\alpha}{\beta}), (\pm\frac{\alpha}{\beta}\sqrt{2(\frac{B_0\beta}{\alpha^2}+1)}, 0, -\frac{\alpha}{\beta}). \tag{4.3}$$

Elliptic points are points that have closed, usually elliptic, trajectories around them in phase space. These elliptic points can cause the motion to become chaotic. However, these points are never reached at energies and trap parameters that are investigated in this work. Furthermore, there are four additional saddle points, located at

$$\begin{aligned}(x,y,z) = (0, \pm\frac{\alpha}{\beta}(2\frac{B_0\beta}{\alpha^2} - 4 + 2\sqrt{5-4\frac{B_0\beta}{\alpha^2}})^{1/2}, \frac{\alpha}{2\beta}(\sqrt{5-4\frac{B_0\beta}{\alpha^2}}-1)), \\ (\pm\frac{\alpha}{\beta}(2\frac{B_0\beta}{\alpha^2} - 4 + 2\sqrt{5-4\frac{B_0\beta}{\alpha^2}})^{1/2}, 0, -\frac{\alpha}{2\beta}(\sqrt{5-4\frac{B_0\beta}{\alpha^2}}-1)).\end{aligned} \tag{4.4}$$

These points can be reached at high bias field and high energies, as will be discussed in Section 4.4.1.

4.2.2 Energy Distribution

When the system is sufficiently ergodic, the distribution of atoms in the trap is only determined by their energy. The harmonic potential is strictly speaking not ergodic, but

the higher-order terms that have been neglected break the symmetry of expression (4.2) and ensure that the condition of sufficient ergodicity is fulfilled. The density of states of a Ioffe quadrupole trap is given by [27]:

$$\rho(\varepsilon) = \frac{(2m\pi^2)^{3/2}}{(2\pi\hbar)^3 2\alpha^2\beta^{1/2}}(\varepsilon^3 + 2\mu B_0 E^2). \tag{4.5}$$

This result is obtained by using potential (4.1) without the terms $\frac{1}{4}\beta^2(x^2+y^2)^2$ and $2\alpha\beta(x^2-y^2)z$, in the defining integral for $\rho(\varepsilon)$:

$$\rho(\varepsilon) \equiv (2\pi\hbar)^{-3}\int d^3r d^3p \delta(\varepsilon - U(x,y,z) - p^2/2m). \tag{4.6}$$

In thermal equilibrium the energy distribution function is a Boltzmann distribution:

$$f(\varepsilon) = n_0\Lambda^3 e^{(-\varepsilon/k_BT)}, \tag{4.7}$$

where Λ is the thermal de Broglie wavelength and n_0 is the density at the trap center, given by [21]:

$$n_0 = \frac{N}{\pi^{3/2}}\frac{(\mu\beta/k_BT)^{1/2}(\mu\alpha/k_BT)^2}{3+2\mu B_0/k_BT}e^{-\mu B_0/k_BT}. \tag{4.8}$$

The density of states can be used together with the distribution function to obtain the energy of an atom cloud in a IQ trap. This internal energy is defined by:

$$E \equiv \int d\varepsilon \varepsilon \rho(\varepsilon) f(\varepsilon). \tag{4.9}$$

This integral can be evaluated and yields:

$$E = (\frac{12 + 6\frac{\mu B_0}{k_BT}}{3 + 2\frac{\mu B_0}{k_BT}})Nk_BT, \tag{4.10}$$

with N the number of atoms. In the harmonic limit $k_BT \ll \mu B_0$ there is equipartition of potential and kinetic energy, they both contribute $\frac{3}{2}k_BT$ to the internal energy. In the limit $k_BT \gg \mu B_0$, which makes the potential approximately linear, the ratio of potential and kinetic energy is 5/3.

4.3 Simulation

The question that the simulations have to answer is on what timescale collisionless motion can re-establish an equilibrium of the energy distribution after energy has been added to only one of the dimensions. The starting point of a simulation is an atom cloud in equilibrium in a harmonic trap. Atom clouds are used as they give an average behavior of atoms. Using single atoms would yield exact trajectories in phase space, but the result

Number of atoms	N	$5 \cdot 10^3$
Ramping time	t_{ramp}	50ms
Magnetic bias field ($t = 0$)	$B_{0,begin}$	99.6G
Magnetic bias field ($t > t_{ramp}$)	$B_{0,end}$	1.5G
Magnetic field gradient	α	$1.0 \cdot 10^4$G/m
Magnetic field curvature	β	$47.5 \cdot 10^4$G/m^2

Table 4.1: *Default values of parameters used in the simulation.*

would be dependent on the initial position and velocity of the atom, something that does not have to be taken into account when working with clouds. Two kinds of clouds have been used, namely thermal clouds and clouds in which all the atoms have the same energy. The former is used to compare the results of the simulations with experiments while the latter is used to gain a better understanding of the dynamics of atoms at a certain energy.

During the simulation the position and velocity of each atom is determined as a function of time by integrating the equations of motion. How the initial position and velocity of atoms in a cloud are determined is described in Appendix C. At the start of the simulation the magnetic bias field B_0 is adiabatically ramped down, thereby increasing the energy of the atoms in the radial direction. The ramping is adiabatic if the condition $\frac{1}{\omega_r^2}\frac{d\omega_r}{dt} < 1$ is fulfilled [33]. The ideal continuous ramp is approximated by a number of steps, which are short enough to keep the ramping adiabatic. This approach has been chosen because that is how the experiments are performed. The output of the program is the total energy, rms-widths of the cloud and the kinetic energies in every direction as a function of time. With the rms-widths a comparison with experiments can be made, and with the kinetic energies in different directions the transfer of energy from one direction to the other can be determined.

4.4 Results

In the simulations a number of parameters can be changed, for example the magnetic field gradient or the ramping time. The dependence of trap frequencies or characteristic mixing time on one of these parameters is investigated while all other parameters are kept constant. The default values of the parameters are the ones that are being used in the experiment. These values are given in Table 4.1. The energy of atoms in the next Sections is given as a temperature, with total energy given by $E_{tot} = E_{kin} + E_{pot} = 3k_BT$.

4.4.1 Single-atom Results

Simulating the motion of a single atom in the trap is a starting point for simulations with more atoms, but also gives useful information on trap frequencies and energy increase as a result of the ramping of the bias field.

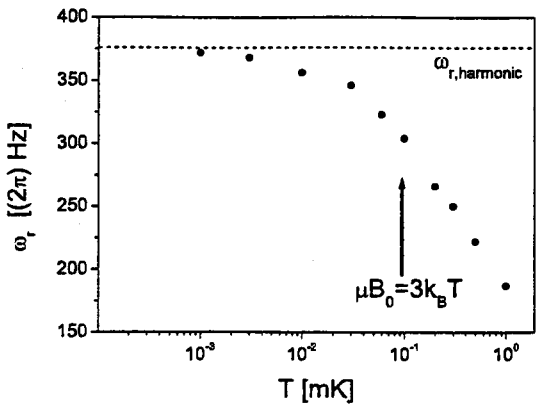

Figure 4.1: *Radial trap frequency of an atom with energy $3k_BT$, at a bias field of $B_0 = 1.5G$.*

Trap frequencies are obtained from plotting position as a function of time and averaging over many oscillation periods. In Figure 4.1 the radial trap frequency as a function of atomic energy is shown. The bias field was not ramped here, but was kept constant at a value of 1.5G. For energies much smaller than the potential energy in the trap center μB_0 the trap frequency matches its theoretical value of $\omega_r = (2\pi\cdot)376$Hz, for larger energies the trap frequency has an approximately linear dependence on the energy. The axial trap frequency is $\omega_z = (2\pi\cdot)44.7$Hz for all atomic energies considered.

Ramping the bias field adds energy to every atom because it increases the radial trap frequency, $\omega_r \sim B_0^{-1/2}$. In Figure 4.2 the relative amount of energy that is added to an atom is shown as a function of the atomic energy. The lower this energy is, the more it is

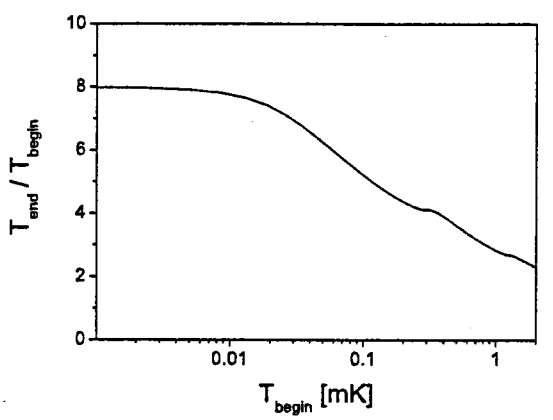

Figure 4.2: *Relative amount of energy added to an atom by ramping the bias field from 99.6G to 1.5G.*

affected by the ramping because the change in the magnetic field occurs at $r = 0$ and the time spent near $r = 0$ is inversely proportional to the energy of the atom.

What can also be checked is when the amplitude of oscillation of an atom is large enough to reach a singular point. Comparing the oscillation amplitude with expressions (4.3) and (4.4) yields that for atoms that have an energy below ($3k_B$·)2mK and trap parameters as in Table 4.1 the elliptic points are not reached, while the saddle points can be reached for bias field larger than 55G. For an atom of 1.5mK at a bias field of 55G its oscillation amplitude is approximately 8mm, equal to the distance of saddle points (4.4) from the center at trap parameters as in Table 4.1. That the saddle points are really reached by the atoms can be checked with atom cloud simulations, where at bias fields >55G increases in cloud diameter are observed while the total potential energy stays constant. This is only possible if saddle points play a role in the atom dynamics.

4.4.2 Atom Cloud Dynamics

Atom behavior depends strongly on energy and initial position of the atom. Clouds of typically 10^4 atoms with all the same energy have been used to obtain characteristic times for the exchange of energy between the axial and radial dimensions. By using that many atoms the influence of their initial positions is negligible and an average behavior of an atom with a certain energy is obtained. The results can be used to qualitatively understand what happens in a thermal cloud.

In Figure 4.3 the kinetic energy in the radial direction is shown as a function of time for a cloud with an initial temperature of 700μK. The mixing time is now determined by fitting an exponential decay to the data with $t > t_{ramp}$. An exponential decay is chosen because it gives a reasonable description of the actual data and because relaxation of systems close to equilibrium is often exponential, for instance in transient effects in electrical systems

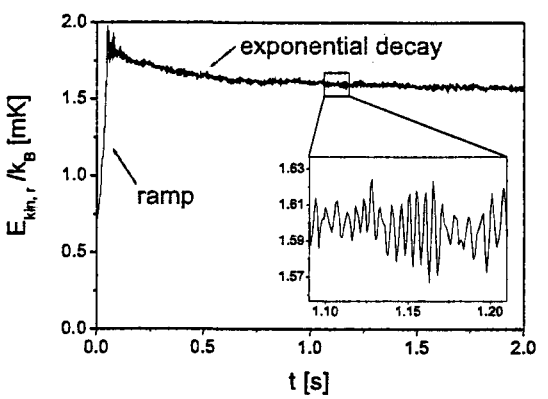

Figure 4.3: *Energy per atom in radial direction as a function of time. The bias field is ramped in 50ms,* $2 \cdot 10^4$ *atoms are used.*

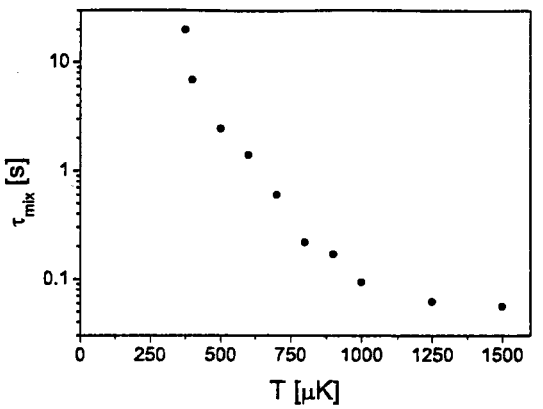

Figure 4.4: *Mixing time as a function of the energy per atom, $E = 3k_BT$.*

or in chemical rate equations[24]. The slight oscillations in energy, shown in the inset of Figure 4.3, are a result of an initial distribution where due to the finite number of atoms there is a deviation from equilibrium between potential and kinetic energy in the same direction. These oscillations have a frequency of $2\omega_r$, which indicates that it is a breathing mode [35]. The oscillations can be decreased by increasing the number of atoms in the simulation. An increase in oscillation amplitude can be seen if the ramping is non-adiabatic. The energy dependence of the mixing time is shown in Figure 4.4. At energies above 1.5mK the mixing occurs very fast. The timescale is then determined by $\tau_{mix} = \frac{1}{2}\omega_z^{-1}$ and is energy-independent. At energies below 350μK mixing is not observed on timescales up to 30s. Even longer timescales have not been considered because they

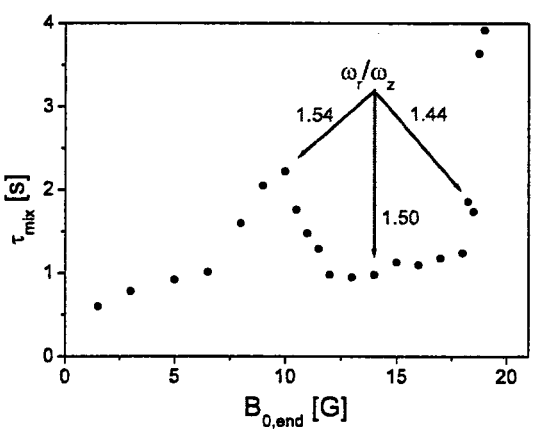

Figure 4.5: *Mixing time as a function of bias field after ramping. Atomic energy is $T = 700\mu K$.*

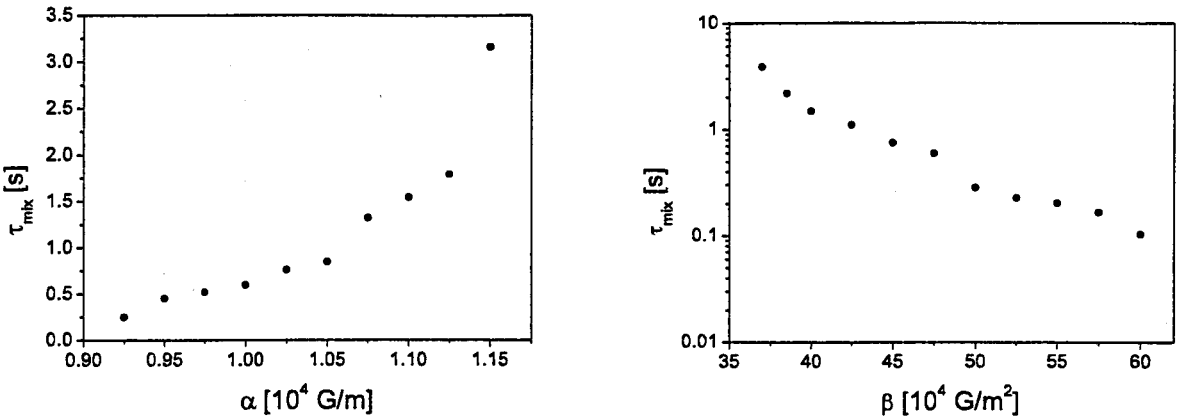

(a) (b)

Figure 4.6: *a) Mixing time as a function of magnetic gradient in radial direction α. b) Mixing time as a function of magnetic curvature in axial direction β.*

exceed the experimental lifetime of our atom trap, the effect becomes negligible compared to the effect of collisions and because of the required computing time.

The mixing time can also be determined as a function of the trap parameters $B_{0,end}$, α and β. In Figure 4.5 the dependence of the mixing time on the bias field after the ramp is shown. The expected trend is that at higher final bias field the mixing time becomes longer, because then the term B_0^2 in potential (4.1) becomes larger and as a result of that the trap is more harmonic. As can be seen there is a strong deviation from this expectation around $B_{0,end} = 14$G. At that point a resonance occurs, which can be understood by looking at the trap frequencies there; $\omega_z = 44.7(2\pi)$Hz and $\omega_r = 67.1(2\pi)$Hz. This means the ratio of the two frequencies is 3/2 at that point. An analytical model explaining this resonance is discussed in Section 4.5.

The mixing time as a function of α and β is shown in Figure 4.6. The dependence of τ_{mix} on α is approximately linear between 0.925 and $1.125 \cdot 10^4$G/m. This can be explained by looking at potential (4.1) again. The radial harmonic term $(x^2 + y^2)$ is proportional to α^2 while the coupling term is proportional to α, therefore the relative importance of the coupling term is $\sim \alpha^{-1}$. An additional effect is that at larger α the oscillation amplitude of the atoms becomes smaller, thereby reducing the importance of the coupling even more. The dependence of the mixing time on β is such that τ_{mix} decreases when β increases. This is the expected behavior when considering the relative importance of the terms in (4.1) again.

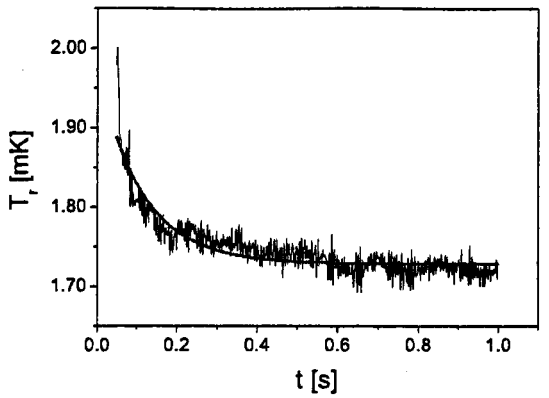

Figure 4.7: *Radial temperature as a function of time for a thermal cloud with an initial temperature of 1mK and 10^4 atoms. The exponential fit is also shown; the temperature during the ramping of the bias field is left out.*

4.4.3 Thermal Cloud Dynamics

The dependence of the behavior of a thermal cloud, i.e. a cloud where the atoms have a thermal energy distribution instead of all the atoms having the same energy, on trap parameters and cloud temperature is much less strong. When α and B_0 are varied over the same range as in Figures 4.5 and 4.6(a) the mixing time stays within the range $100-130$ms. Only when β is decreased there is a significant change in mixing time; $\tau_{mix} \approx 400$ms when $\beta = 37.5 \cdot 10^4 \mathrm{G/m^2}$. The reason for this weak dependence on trap parameters is that a significant part of the energy of the cloud is carried by atoms that are in a regime where mixing does not occur or where it occurs on a timescale of $\frac{1}{2}\omega_z^{-1}$.

An example of the temperature evolution of a thermal cloud after ramping the bias field is shown in Figure 4.7. The first few tens of milliseconds show a linear decrease of temperature, this is determined by the atoms that mix on a timescale of $\frac{1}{2}\omega_z^{-1}$. After that, the decrease is approximately exponential, with a mixing time of 112ms for this particular cloud with a temperature of 1mK and a relative change in temperature of 8%. This result can be used to compare the simulation with an experiment.

4.4.4 Experiment

An experiment in which the bias field of the MT was ramped from 99.6G to 1.5G, that was aimed at determining the scattering length, has been performed. The MOT was operated at a detuning of -2Γ and an intensity of $0.5\mathrm{mW/cm^2}$ for the three MOT beams together. After turning of the MOT a 50μs spin polarization pulse was given and then the MT was turned on. The atom cloud now had a temperature of approximately 1mK and about $1 \cdot 10^9$ atoms. After turning on the MT there was a delay time of 100ms before ramping the bias field, in order to allow the atom cloud to reach its equilibrium state in the MT. Absorption

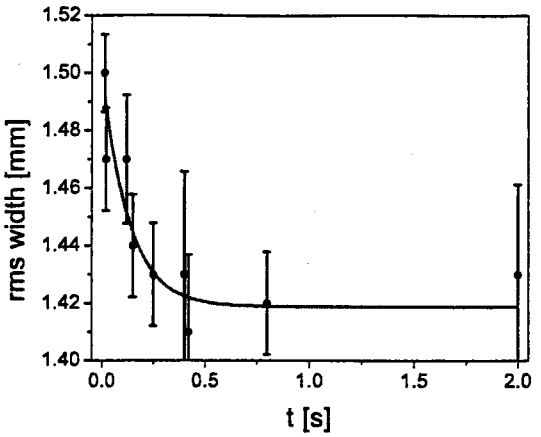

Figure 4.8: *Rms-width of the atom cloud as a function of time. The initial temperature in the MT is* $1.0 \pm 0.1mK$.

imaging was used to determine the cloud radius as a function of time after the ramping. The same measurements have also been done with the channeltron to determine the radial temperature as a function of time, but with less satisfactory results. The result of one series of measurements is shown in Figure 4.8. The exponential fit gives a characteristic equilibration time of 129 ± 25ms and a relative change in width of $5 \pm 3\%$. This can be compared to the simulation result as shown in Figure 4.7. The mixing time and relative change in signal match the experiment to within experimental error. This means that the contribution of collisions to the observed equilibration time is so small that it is within experimental error. Considering the recently measured scattering length of $32 \pm 6a_0$ for $^{20}Ne^*$ [19], an estimation of the collision time can be made:

$$\tau_{coll} = (\overline{n\sigma v})^{-1} = 2.5s, \tag{4.11}$$

where $\overline{n} = n_0/\sqrt{8}$ is the mean density [31] and $\overline{v} = \sqrt{8k_BT/\pi m}$ is the mean velocity. The conclusion can therefore be drawn that collisions do not contribute significantly to the equilibration.

4.5 Resonance Model

The dynamics of a single atom moving in the trapping potential (4.1) can be described by a system of one-dimensional coupled oscillators. In a system of coupled oscillators the rate of transfer of energy from one oscillator to another can be greatly enhanced if the ratio of the two oscillation frequencies is that of two prime numbers [36]. This is exactly the kind of resonance that is shown in Figure 4.5. A representation of the coupled oscillator model is shown in Figure 4.9.

A simple picture of a what happens physically on resonance may be helpful in order to understand why the dynamics of the system change there. The principal difference between a resonance and a non-resonance situation is that on resonance the orbit of the atom is quasi-periodic, with a period of the smallest common multiple of the two oscillation periods. When the force applied to the atom by the coupling term of the potential yields a non-zero result over a single period, the effect over a longer time keeps increasing. In the non-resonance case however the force over a longer time averages out and gives rise to a much smaller effect. The following example may provide some insight into the relation between the coupling term and the resonance frequencies. Take for instance a coupling term x^2z and oscillating motion with frequency ω_x in the x-direction and ω_z in the z-direction. Now the effect of the coupling term can be evaluated:

$$\begin{aligned} F_z &\sim x^2 \sim \cos^2(\omega_x t) \sim \cos(2\omega_x t) + 1, \\ F_x &\sim xz \sim \cos(\omega_x t)\cos(\omega_z t) \sim \cos((\omega_x + \omega_z)t) + \cos((\omega_x - \omega_z)t). \end{aligned} \tag{4.12}$$

This situation can be compared to a single one-dimensional oscillator, where resonance occurs if an external force applied to the atom has the eigenfrequency of the atom, $F_x \sim \cos(\omega_x)$ and $F_z \sim \cos(\omega_z)$. From (4.12) it can be seen that this happens only when $\omega_z = 2\omega_x$.

A question that arises when the basic picture of the coupled oscillator system is considered is: why does the energy that is transferred to the other direction not return again after a certain time? For two linear oscillators this 'sloshing' of energy is a well-known phenomenon. The system that is discussed here is nonlinear in nature however. There is a fundamental difference between linear and nonlinear coupled oscillators; the oscillation frequencies of the former do not depend on the energies in the oscillation directions while those of the latter do. Figure 4.1 shows the dependence of the radial trap frequency on

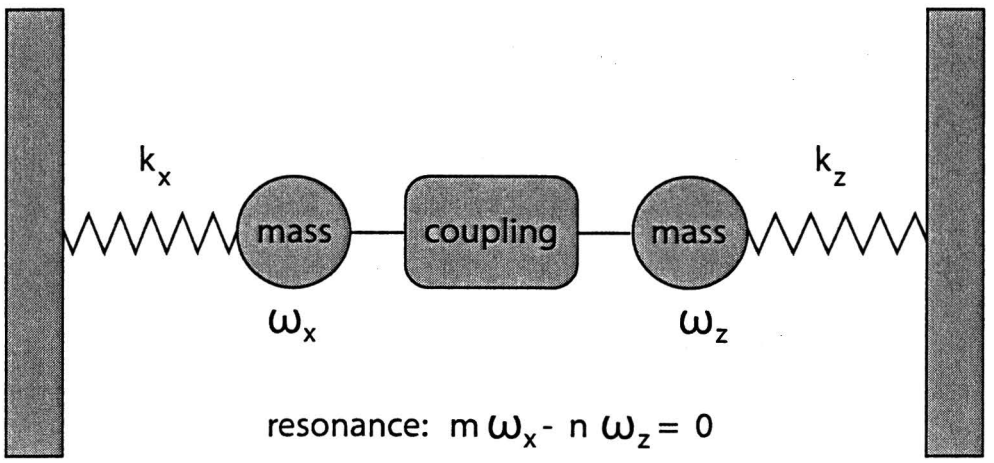

Figure 4.9: *Schematic picture of the coupled oscillator model. Two one-dimensional oscillators with frequencies ω_x and ω_z can exchange energy through a coupling.*

the energy and thereby that nonlinear nature. This means that in the nonlinear case the atom can be shifted out of resonance when energy is transferred from one direction to the other. Therefore, if the resonance occurs when the energy difference between the axial and radial directions is at a maximum, then the system will move away from resonance as it comes closer to its equilibrium state.

When the ratio of the frequencies is given as $m : n$, the order of the resonance is $m+n$. Resonances of order five or more are called high order resonances; their timescale is usually long compared to the characteristic timescale of the system (such as ω_r^{-1}) [37].

The resonances that occur in a Hamiltonian system and their relative importance can be obtained by transforming the Hamiltonian to Birkhoff-Gustavson normal form [36, 38]. This normalization is a general method to find resonances in Hamiltonian systems. The idea is to separate the Hamiltonian into a normal form that gives rise to regular uncoupled motion and a polynomial that describes resonant interactions between the degrees of freedom:

$$H = H_0(\tau_1, \tau_2) + \varepsilon H_{res}(q_1, q_2, p_1, p_2), \tag{4.13}$$

where $\tau_i = \frac{1}{2}(q_i^2 + p_i^2)$ and ε a small parameter describing the strength of the interaction.

For one atom in a magnetic trap the Hamiltonian is given by:

$$H(x, y, z, p_x, p_y, p_z) = \frac{1}{2m}(p_x^2 + p_y^2 + p_z^2) + U(x, y, z), \tag{4.14}$$

where p_x, p_y, p_z are the momenta in the three dimensions and $U(x, y, z)$ is the potential given by (4.1). In order to be able to explain a fifth order resonance the potential has to be linearized up to fifth order:

$$\begin{aligned} U(x,z) =& \mu[\frac{\alpha^2 - B_0\beta}{2B_0}x^2 + \frac{\alpha\beta}{3B_0}z^2 + \frac{\alpha\beta}{3B_0}x^2 z - \frac{(\alpha^2 - B_0\beta)\beta}{12B_0^2}x^2 z^2 \\ & - \frac{\alpha\beta(\alpha^2 - B_0\beta)}{10B_0^3}x^4 z - \frac{\alpha\beta^2}{10B_0^2}x^2 z^3]. \end{aligned} \tag{4.15}$$

Here the terms containing y have been left out because the potential is symmetric in x and y, except for a single minus sign in the coupling term that does not have an effect on resonances that can occur or on their relative importance. The variables x, p_x and z, p_z are now transformed to the new complex variables a_+, a_- and b_+, b_-:

$$\begin{aligned} a_\pm &= (m\omega_z)^{1/2} z \pm i(m\omega_z)^{-1/2} p_z, \\ b_\pm &= (m\omega_x)^{1/2} x \pm i(m\omega_x)^{-1/2} p_x. \end{aligned} \tag{4.16}$$

Here the position is scaled by $(m\omega)^{-1/2}$ and the momentum by the inverse of that. The position and momentum have to be scaled by quantities that are each other's inverse in order to leave the commutator of the two $[x, p_x]$ unchanged. The Hamiltonian can now be

$\omega_x : \omega_z$	Resonant term	Order
1 : 2	ab^2	3
1 : 1	a^2b^2	4
3 : 2	a^3b^2	5
1 : 4	ab^4	5

Table 4.2: *Resonances occurring in the energy transfer between the x- and z-dimensions in the magnetic trap, ordered in descending importance. The resonant terms are obtained from (4.17).*

expressed as

$$\begin{aligned} H(a_+, a_-, b_+, b_-) = {} & \frac{1}{2}\omega_z a_+ a_- + \frac{1}{2}\omega_x b_+ b_- + \frac{\mu\alpha\beta}{24B_0 m^{3/2}\omega_x \omega_z^{1/2}}(a_+ + a_-)(b_+ + b_-)^2 \\ & - \frac{\mu(\alpha^2 - B_0\beta)\beta}{192B_0^2 m^2 \omega_x \omega_z}(a_+ + a_-)^2(b_+ + b_-)^2 - \frac{\mu\alpha(\alpha^2 - B_0\beta)}{320B_0^3 m^{5/2}\omega_x^2 \omega_z^{1/2}}(a_+ + a_-)(b_+ + b_-)^4 \\ & - \frac{\mu\alpha\beta}{320B_0^2 m^{5/2}\omega_x \omega_z^{3/2}}(a_+ + a_-)^3(b_+ + b_-)^2, \end{aligned} \tag{4.17}$$

where the first two terms are in Birkhoff normal form and the other terms are called resonant terms. The powers of the operators in the resonant terms indicate which resonances are present in the system, for example the $(a_+ + a_-)(b_+ + b_-)^4$ term indicates that a resonance occurs if $\omega_x : \omega_z = 1 : 4$. The order of the resonance determines its importance, lower order indicating a more important resonance. A qualitative ordering of the resonances is given in Table 4.2. Due to the values of the trap parameters α, β and B_0 and the atomic energies in the trap the radial trap frequency is always larger than the axial one. The most important resonance that has that property is the 3 : 2 resonance, the one observed in the simulations and shown in Figure 4.5.

An important characteristic of the potential is that it is symmetric in x, but not in z. The consequence is that the operators b_+, b_- can only occur in even powers, whereas the operators a_+, a_- are not subject to that restriction. This explains why for instance the $\omega_x : \omega_z = 2 : 1$ does not occur and the $\omega_x : \omega_z = 1 : 2$ does.

Chapter 5

Conclusion

The common denominator of the work described in the previous Chapters is the search for elastic collisions. Observing these collisions experimentally requires first of all an increased collision rate. In order to obtain a sufficiently large collision rate, the temperature had to be decreased and the number of atoms increased. The increase in number of atoms by optimizing the transfer of atoms from the MOT to the MT was successful, as described in Section 2.3. A further increase in number of atoms requires more laser power to increase the loading rate of the MOT. Decreasing the temperature of the atom cloud by means of optical molasses has been shown to work. However, the gain in temperature after equilibration in the magnetic trap was very small. The critical factor in reaching low temperature in the MT after the application of optical molasses is the exact matching of the MT to the temperature, size and position of the atom cloud. In practice this is very hard to achieve.

Another, more promising approach to reduce the temperature is to apply optical molasses in the MT, a technique recently developed by Schmidt *et.al.* [39]. Because the atoms have to stay in the $|m_J = +2\rangle$ state the cooling can only be done with a one-dimensional $\sigma^+ - \sigma^+$ beam along the axial axis of the trap, but it would make matching the MT to the atom cloud unnecessary. It is expected that with this technique the temperature can be reduced to 200μK, the Doppler temperature. This would increase the collision rate an order of magnitude, enough to measure elastic collisions. Another advantage is that the anharmonic mixing is completely suppressed at this temperature.

Measuring the the scattering length can be done by either the two knives experiment, described in Chapter 3, or by observing collisional redistribution of energy after ramping the bias field as described in Chapter 4. Of the two methods, the latter appears to be the more promising one under present experimental conditions. The two knives experiment requires many more collisions than the collisional redistribution and is therefore still far out of reach. By implementing the above-mentioned cooling technique in the MT, the conditions should become sufficient to measure collisional redistribution of energy.

Anharmonic mixing is a process that is usually undesirable. In Chapter 4 the timescales on which it takes place have been determined, thereby indicating conditions under which the effect is small enough to be able to measure elastic collisions. It is also conceivable that anharmonic mixing can be used constructively. For example if the molasses in the

MT results in cooling only in the axial direction, the mixing rate can be enhanced by choosing the right trap parameters in order to be able to reach a lower temperature in the radial direction as well. Resonances in the mixing rate as described in Section 4.5 could be particularly useful in that respect.

Bibliography

[1] S.N. Bose. *Z. Phys*, 26:178, 1924.

[2] A. Einstein. *Sitzber. Kgl. Preuss. Akad. Wiss.*, page 261, 1924.

[3] K.B. Davis. M.O. Mewes. M.R. Andrews. N.J. van Druten. D.S. Durfee. D.M. Kurn. and W. Ketterle. Bose-einstein condensation in a gas of sodium atoms. *Phys. Rev. Lett*, 75:3969, 1995.

[4] M. Anderson. J.R. Ensher. M.R. Matthews. C.E. Wieman. and E.A. Cornell. Observation of bose-einstein condensation in a dilute atomic vapor. *Science*, 269:198, 1995.

[5] S.L. Cornish. N.R. Claussen. J.L. Roberts. E.A. Cornell. and C.E. Wieman. Stable $^{8}5$rb bose-einstein condensates with widely tunable interactions. *Phys. Rev. Lett.*, 85:1795, 2000.

[6] J.J. Pillet. C.C. Bradley. C.A. Sackett and R. Hulet. Evidence of bose-einstein condensation in an atomic gas with attractive interactions. *Phys. Rev. Lett.*, 75:1687, 1995.

[7] D.G. Fried. T.C. Killian. L. Willmann. D. Landhuis. S.C. Moss. D. Kleppner. and T.J. Greytak. Bose-einstein condensation of atomic hydrogen. *Phys. Rev. Lett.*, 81:3811, 1998.

[8] A. Robert. O. Sirjean. A. Browaeys. J. Poupard. S. Nowak. D. Boiron. C.I. Westbrook. and A. Aspect. A bose-einstein condensate of metastable atoms. *Science*, 292:461, 2001.

[9] G. Modugno. G. Ferrari. G. Roati. R.J. Brecha. A. Simoni. and M. Inguscio. Bose-einstein condensation of potassium atoms by sympathetic cooling. *Science*, 294:1320, 2001.

[10] T. Weber. J. Herbig. M. Mark. H.C. Nägerl. and R. Grimm. Bose-einstein condensation of cesium. *Science*, 299:232, 2003.

[11] Y. Takasu. K. Maki. K. Komori. T. Takano. K. Honda. M. Kumakura. T. Yabuzaki. and Y. Takahashi. Spin-singlet bose-einstein condensation of two-electron atoms. *Phys.Rev.Lett.*, 91:040404, 2003.

[12] S. Jochim. M. Bartenstein. A. Altmeyer. G. Hendl. S. Riedl. C. Chin. J. Hecker Denschlag. and R. Grimm. Bose-einstein condensation of molecules. *Science*, 302:2101, 2003.

[13] M. Greiner. C.A. Regal. and D.S. Jin. A molecular bose-einstein condensate emerges from a fermi sea. *cond-mat*, page 0311172, 2003.

[14] M. Zinner. P. Spöden. T. Kraemer. G. Birkl. and W. Ertmer. Precision measurement of the $^3p_2$ lifetime of neon. *Phys. Rev. A*, 67:1, 2003.

[15] J.G.C. Tempelaars. *Trapping metastable neon atoms.* PhD thesis, Eindhoven University of Technology, Group of Theoretical and Experimental Atomic Physics and Quantum Electronics, 2001.

[16] H.J. Metcalf. and P. van der Straten. *Laser Cooling and Trapping.* 1999.

[17] W.H. Wing. On neutral particle trapping in quasistatic electromagnetic fields. *Prog. Quant. Electr.*, 8:181, 1984.

[18] N.V. Vitanov. and B.M Garraway. Landau-zener model: Effects of finite coupling duration. *Phys. Rev. A*, 53:6, 1996.

[19] P. Spöden. Private communication, september 2003.

[20] C. Cohen-Tannoudji. *Cours de Physique Atomique et Moleculaire.* 1996.

[21] R. Stas. Laser cooling and trapping of metastable neon atoms. Master's thesis, Eindhoven University of Technology, Group of Theoretical and Experimental Atomic Physics and Quantum Electronics, 1999.

[22] V.P. Mogendorff. Towards bec of metastable neon. Master's thesis, Eindhoven University of Technology, Group of Theoretical and Experimental Atomic Physics and Quantum Electronics, 2000.

[23] A. Browaeys. A. Robert. O. Sirjean. J. Poupard. S. Nowak. D. Boiron. C.I. Westbrook. and A. Aspect. Thermalization of magnetically trapped metastable helium. *Phys. Rev. A*, 64:034703, 2001.

[24] Chandler. *Introduction to Modern Statistical Mechanics.* 1987.

[25] M. Köhl. M.J. Davis. C.W. Gardiner. T.W. Hänsch. and T. Esslinger. Growth of bose-einstein condensates from thermal vapor. *Phys. Rev. Lett.*, 88:080402, 2002.

[26] Y. Shin. A. Schirotzek. T.A. Pasquini. A.E. Leanhardt. D.E. Pritchard. and W. Ketterle. Distillation of bose-einstein condensates in a double-well potential. *cond-mat*, page 0311514, 2003.

[27] O.J. Luiten. M.W. Reynolds. and J.T.M. Walraven. Kinetic theory of evaporative cooling of a trapped gas. *Phys. Rev. A*, 53:381, 1996.

[28] B.J. Claessens. Preparations for evaporative cooling of magnetically trapped Ne^*. Master's thesis, Eindhoven University of Technology, Group of Theoretical and Experimental Atomic Physics and Quantum Electronics, 2002.

[29] D.W. Snoke. and J.P. Wolfe. Population dynamics of a bose gas near saturation. *Phys. Rev. B*, 39:4030, 1989.

[30] C.R. Monroe. E.A. Cornell. C.A. Sackett. C.J. Myatt. and C.E. Wieman. Measurement of cs-cs elastic scattering at $t = 30\mu k$. *Phys. Rev. Lett.*, 70:414, 1993.

[31] H. Wu. E. Arimondo. and C.J Foot. Dynamics of evaporative cooling for bose-einstein condensation. *Phys. Rev. A*, 56:560, 1997.

[32] P.W. Pinkse. A. Mosk. M. Weidemüller. M.W. Reynolds. and T.W. Hijmans. One-dimensional evaporative cooling of magnetically trapped hydrogen. *Phys. Rev. A*, 57:4747, 1998.

[33] E.L. Surkov. J.T.M. Walraven. and G.V. Shlyapnikov. Collisionless motion of neutral particles in magnetic traps. *Phys. Rev. Lett.*, 49:4778, 1994.

[34] T. Bergeman. G. Erez. and H.J. Metcalf. Magnetostatic trapping fields for neutral atoms. *Phys. Rev. A*, 35:1535, 1985.

[35] J.W. Gadzuk. Breathing mode excitation in near-harmonic systems: resonant mass capture, desorption and atoms in optical lattices. *J. Phys. B*, 31:4061, 1998.

[36] J.M. Tuwankotta. and F. Verhulst. Symmetry and resonance in hamiltonian systems. *J. Appl. Math.*, 61:1369, 2000.

[37] J.M. Tuwankotta. and G.R.W. Quispel. Geometric numerical integration applied to the elastic pendulum athigher order resonance. *Journal of Computational and Applied Mathematics*, 154:229, 2003.

[38] G.W. Bluman. and S.C. Anco. *Symmetry and integration methods for differential equations.* 2002.

[39] P.O. Schmidt. S. Hensler. J. Werner. T. Binhammer. A. Görlitz. and T. Pfau. Doppler cooling of an optically dense cloud of trapped atoms. *quant-ph*, page 0208129, 2002.

[40] K.A.H. van Leeuwen. *Lasers in fysische experimenten.* 1987.

[41] M. Hoogerland. *Laser Manipulation of Metastable Neon Atoms.* PhD thesis, Eindhoven University of Technology, Group of Theoretical and Experimental Atomic Physics and Quantum Electronics, 1993.

[42] L. Vestergaard Hau. S.E. Harris. Z. Dutton. and C.H. Behroozi. Light speed reduction to 17 metres per second in an ultracold atomic gas. *Nature*, 397:594, 1999.

[43] D. F. Phillips. A. Fleischhauer. A. Mair. and R. L. Walsworth. Storage of light in atomic vapor. *Phys. Rev. Lett.*, 86:783, 2001.

Appendix A

Runaway Evaporative Cooling

In this Appendix the conditions that are needed in order to reach the runaway regime of the evaporative cooling process are determined. This derivation was developed by Cohen-Tannoudji [20] and is based on a thermodynamic description of the evaporative cooling process, implying that close to the BEC transition this description loses its validity. It is assumed that the cooling is performed in such a way that the truncation parameter $\eta = \varepsilon_t / k_B T$ is kept constant. The starting point is a commonly used set of equations for the time evolution of the energy, temperature and number of atoms of an atom cloud:

$$\begin{aligned} \frac{\dot{E}}{E} &= \frac{\dot{N}}{N} + \frac{\dot{T}}{T}, \\ \frac{\dot{N}}{N} &= -\Gamma_{ev} + \tilde{\xi}\frac{\dot{T}}{T} - \Gamma_{inel}, \\ \frac{\dot{E}}{E} &= -\frac{\eta + \tilde{\kappa}}{\tilde{c}}\Gamma_{ev} + \frac{\tilde{\xi}\eta}{\tilde{c}}\frac{\dot{T}}{T} - \Gamma_{inel}. \end{aligned} \tag{A.1}$$

Here $\Gamma_{ev} = n\sigma v e^{-\eta} V_{ev}/V_e$ is the evaporation rate and Γ_{inel} the inelastic collision rate, $\tilde{\xi} = (\frac{3}{2} + \delta)[1 - R(\frac{3}{2} + \delta, \eta)]$ describes the removal of atoms as a result of lowering ε_t and $\tilde{\kappa} = 1 - \frac{X_{ev}}{V_{ev}}$ and $\tilde{c} = (\frac{3}{2} + \delta)R(\frac{3}{2} + \delta, \eta)$ are constants describing the effect of the truncation of the trap. Here R depends on incomplete gamma functions and V_{ev}, V_e and X_{ev} are reference volumes as described in [27] and δ denotes the dependence of the potential on the distance from the center, $U \sim r^{3/\delta}$. Of all these quantities, Γ_{ev} is the only one that is not constant because it depends on the collision rate. It is now useful to eliminate $\frac{\dot{E}}{E}$: (A.1) simplifies to:

$$\begin{aligned} \frac{\dot{N}}{N} &= -\frac{1}{\tilde{\alpha}}\frac{\dot{T}}{T} - \Gamma_{inel}, \\ \frac{\dot{N}}{N} &= -\Gamma_{ev} + \tilde{\xi}\frac{\dot{T}}{T} - \Gamma_{inel}, \end{aligned} \tag{A.2}$$

where $\tilde{\alpha}$ is defined as $\tilde{\alpha} = \frac{\eta + \tilde{\kappa} - \tilde{c}}{\tilde{c} + \tilde{\kappa}\tilde{\xi}}$. Now (A.2) describes the change in number of atoms and temperature during an evaporative cooling process, but with respect to the collision

rate it is more interesting what happens to the average density and velocity of the atoms. Therefore (A.2) is rewritten as:

$$\begin{aligned} \frac{\dot{n}}{n} &= \frac{\delta\tilde{\alpha}-1}{1-\tilde{\alpha}\tilde{\xi}}\Gamma_{ev} - \Gamma_{inel}, \\ \frac{\dot{v}}{v} &= \frac{\tilde{\alpha}}{2(1-\tilde{\alpha}\tilde{\xi})}\Gamma_{ev}. \end{aligned} \tag{A.3}$$

These equations can be simplified further to:

$$\begin{aligned} \dot{n} &= An^2v\sigma - \Gamma_{inel}n, \\ \dot{v} &= -Bnv^2\sigma, \end{aligned} \tag{A.4}$$

where A and B are constants defined as:

$$\begin{aligned} A &= \frac{\delta\tilde{\alpha}-1}{1-\tilde{\alpha}\tilde{\xi}}e^{-\eta}\frac{V_{ev}}{V_e}, \\ B &= \frac{\tilde{\alpha}}{2(1-\tilde{\alpha}\tilde{\xi})}e^{-\eta}\frac{V_{ev}}{V_e}. \end{aligned} \tag{A.5}$$

To simplify (A.4) further the equations are now made dimensionless by normalizing all quantities to their value at time $t = 0$. Time itself is normalized to the collision time at $t = 0$. This yields:

$$\begin{aligned} \frac{d\hat{n}}{dt} &= A\hat{n}^2\hat{v} - \frac{\Gamma_{inel}}{n_0\sigma v_0}\hat{n}, \\ \frac{d\hat{v}}{dt} &= -B\hat{n}\hat{v}^2. \end{aligned} \tag{A.6}$$

Because the collision cross section σ is constant the change in the collision rate is determined by the change in nv. That change can easily be determined from (A.6):

$$\frac{d}{d\hat{t}}(\hat{n}\hat{v}) = (A-B)\hat{n}^2\hat{v}^2 - \frac{\Gamma_{inel}}{n_0\sigma v_0}\hat{n}\hat{v}. \tag{A.7}$$

The solution to this equation is given by:

$$\hat{n}\hat{v} = \frac{e^{-\frac{\Gamma_{inel}}{n_0\sigma v_0}}}{1-(1-e^{-\frac{\Gamma_{inel}}{n_0\sigma v_0}})\frac{A-B}{\Gamma_{inel}/n_0\sigma v_0}}. \tag{A.8}$$

It can be seen from this solution that there are three types of behavior for $\frac{d}{d\hat{t}}(\hat{n}\hat{v})$, depending on the ratio of $A-B$ and $\frac{\Gamma_{inel}}{n_0\sigma v_0}$. If $A-B < \frac{\Gamma_{inel}}{n_0\sigma v_0}$ the collision rate is decreasing monotonously, if $A-B = \frac{\Gamma_{inel}}{n_0\sigma v_0}$ it stays constant and if $A-B > \frac{\Gamma_{inel}}{n_0\sigma v_0}$ then the collision rate keeps increasing and solution (A.8) diverges at time:

$$\hat{t}_{div} = -\frac{n_0\sigma v_0}{\Gamma_{inel}}ln(1-\frac{\Gamma_{inel}/n_0\sigma v_0}{A-B}). \tag{A.9}$$

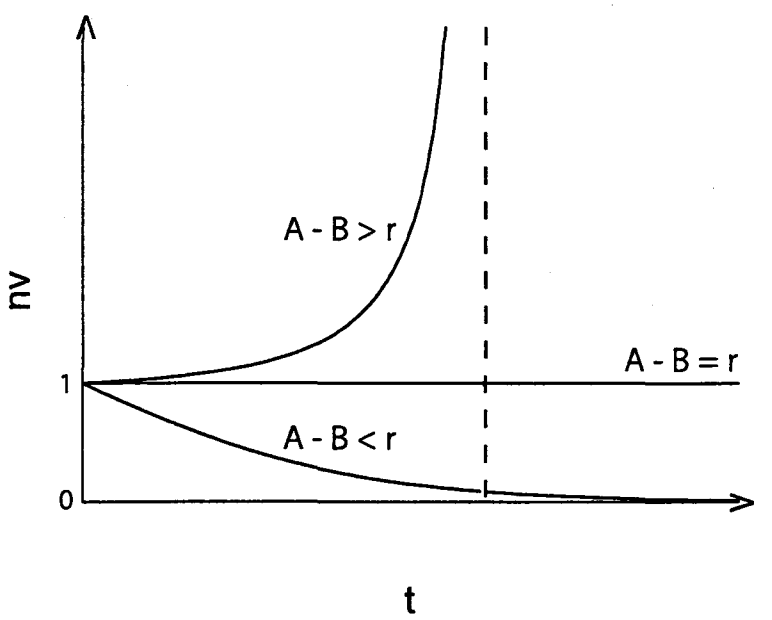

Figure A.1: *The collision rate as a function of time in arbitrary units. The quantity r is defined as* $\frac{\Gamma_{inel}}{n_0 \sigma v_0}$

The solutions to (A.8) for the three regions of $A-B$ are shown in Figure A.1. This diverging of the collision rate is what is meant by the runaway regime of evaporative cooling. The constants A and B depend on the truncation parameter η, and it can be shown that $A-B$ never exceeds 0.0033 [20]. This value is obtained for $\eta = 6$. Now this places a lower limit on the initial collision rate times the trap lifetime $\tau = \Gamma_{inel}^{-1}$. In order to achieve runaway evaporative cooling the number of collisions times the trap lifetime has to exceed 300.

Appendix B

Optical Pumping Model

A model based on rate equations for the occupation of the magnetic sub-states of the ground and excited states of metastable neon will be derived here. These states are shown in Figure B.1. It is assumed here that only σ^+ light is present, therefore the states $m_{J,e} = -3, -2$ do not have to be included in the model. Furthermore, the $m_{J,e} = +3$ state is also not included because for the efficiency of spin polarization it makes no difference whether the atom is in the $m_{J,g} = +2$ or in the $m_{J,e} = +3$ state. This transition is closed and all atoms that are in the $m_{J,e} = +3$ state when the MT is turned off will return to the $m_{J,g} = +2$ state by spontaneous emission.

The bias field that is present causes the effective detuning to change because of the Zeeman effect. The Zeeman shift is different for all four $m_{J,g} \rightarrow m_{J,e}$ transitions and is given by:

$$\delta(B) = \mu_B B(g_e m_e - g_g m_g)/2\pi\hbar. \tag{B.1}$$

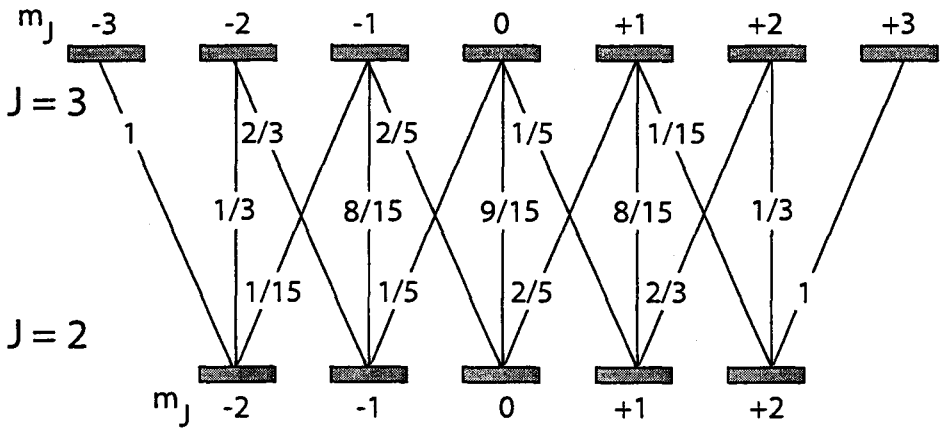

Figure B.1: *The $J = 2$ and $J = 3$ states of metastable neon with the magnetic sub-states $m_J = -J, .., J$. All allowed dipole transitions and their squared Clebsch-Gordan coefficients are also shown.*

The values of g_g and g_e are 3/2 and 11/8 respectively. The photon flux of the spin polarization pulse is given by $j = \frac{I}{\hbar\omega}$, with I in W/m^2. The absorption cross-section for a transition from initial state $|i\rangle$ to final state $|k\rangle$ is given by [40]:

$$\sigma_{ik}(\delta(B)) = \frac{C_{ik}^2}{2J_k+1}|\langle J_k||1||J_i\rangle|^2 e^2 \frac{\pi\omega}{\varepsilon_0\hbar c} L(\delta(B),\Gamma), \tag{B.2}$$

where $|\langle J_k||1||J_i\rangle|^2$ is the reduced matrix element for a dipole transition. This matrix element can be expressed in the linewidth:

$$|\langle J_k||1||J_i\rangle|^2 = \frac{e^2\omega^3}{3\pi\varepsilon_0\hbar c^3}(2J_k+1)\Gamma. \tag{B.3}$$

Now the cross-section only depends on the Clebsch-Gordan coefficient, the wavelength and the detuning:

$$\sigma_{ik}(\delta(B)) = \frac{3C_{ik}^2\lambda^2}{2\pi(1+(2\delta(B)/\Gamma)^2)}. \tag{B.4}$$

With the rate for absorption and stimulated emission $j\sigma_{ik}$ and the spontaneous emission rate $C_{ik}^2\Gamma$ the rate equations can now be formulated:

$$\begin{aligned}
\frac{\partial n_{g,-2}}{\partial t} &= \frac{3I\lambda^2}{2\pi\hbar\omega}\frac{C_{-2,-1}^2}{1+(2\delta(B)/\Gamma)^2}(n_{e,-1}-n_{g,-2}) + C_{-2,-1}^2\Gamma n_{e,-1},\\
\frac{\partial n_{e,-1}}{\partial t} &= \frac{3I\lambda^2}{2\pi\hbar\omega}\frac{C_{-2,-1}^2}{1+(2\delta(B)/\Gamma)^2}(n_{g,-2}-n_{e,-1}) - \Gamma n_{e,-1},\\
\frac{\partial n_{g,-1}}{\partial t} &= \frac{3I\lambda^2}{2\pi\hbar\omega}\frac{C_{-1,0}^2}{1+(2\delta(B)/\Gamma)^2}(n_{e,0}-n_{g,-1}) + C_{-1,0}^2\Gamma n_{e,0} + C_{-1,-1}^2\Gamma n_{e,-1},\\
\frac{\partial n_{e,0}}{\partial t} &= \frac{3I\lambda^2}{2\pi\hbar\omega}\frac{C_{-1,0}^2}{1+(2\delta(B)/\Gamma)^2}(n_{g,-1}-n_{e,0}) - \Gamma n_{e,0},\\
\frac{\partial n_{g,0}}{\partial t} &= \frac{3I\lambda^2}{2\pi\hbar\omega}\frac{C_{0,+1}^2}{1+(2\delta(B)/\Gamma)^2}(n_{e,+1}-n_{g,0}) + C_{0,+1}^2\Gamma n_{e,+1} + C_{0,0}^2\Gamma n_{e,0} + C_{0,-1}^2\Gamma n_{e,-1},\\
\frac{\partial n_{e,+1}}{\partial t} &= \frac{3I\lambda^2}{2\pi\hbar\omega}\frac{C_{0,+1}^2}{1+(2\delta(B)/\Gamma)^2}(n_{g,0}-n_{e,+1}) - \Gamma n_{e,+1},\\
\frac{\partial n_{g,+1}}{\partial t} &= \frac{3I\lambda^2}{2\pi\hbar\omega}\frac{C_{+1,+2}^2}{1+(2\delta(B)/\Gamma)^2}(n_{e,+2}-n_{g,+1}) + C_{+1,+2}^2\Gamma n_{e,+2} + C_{+1,+1}^2\Gamma n_{e,+1} + C_{+1,0}^2\Gamma n_{e,0},\\
\frac{\partial n_{e,+2}}{\partial t} &= \frac{3I\lambda^2}{2\pi\hbar\omega}\frac{C_{+1,+2}^2}{1+(2\delta(B)/\Gamma)^2}(n_{g,+1}-n_{e,+2}) - \Gamma n_{e,+2},\\
\frac{\partial n_{g,+2}}{\partial t} &= C_{+2,+1}^2\Gamma n_{e,+1} + C_{+2,+2}^2\Gamma n_{e,+2}.
\end{aligned} \tag{B.5}$$

The values of the Clebsch-Gordan coefficients [41] are shown in Figure B.1. The coupled equations can now be numerically solved to obtain the occupation numbers for all substates as a function of time.

Appendix C

Particle Distributions

The distributions used in the anharmonic mixing program are created by using random numbers. Exactly how this is done will be shown in this appendix.

The total energy of the distribution is given by:

$$E_{tot} = \int_{E_{min}}^{E_{max}} Ef(E)\rho(E)dE, \tag{C.1}$$

where E_{min} and E_{max} $f(E)$ are the minimum and maximum energies that are taken into account and $\rho(E)$ as in(4.7) and(4.5) respectively. The energy of a real thermal distribution is obtained by integrating from zero to infinity, but when discretizing this distribution a cut-off at a certain energy E_{max} has to be made. This is chosen to be at the point where $E_{tot} = 0.99E_{tot}(\infty)$. Now the energy range is divided into intervals with length $\Delta E = E_{max}/N$, and the N particles are assigned an energy of $(n - 1/2)\Delta E$, where $n = 1...N$. Then for each particle a random number between 0 and 1 determines the ratio of its potential and kinetic energy. This approach is valid as long as the potential is harmonic, because then there is equipartition of potential and kinetic energy.

From the potential energy the coordinates of a particle are determined by placing it on a sphere with radius $r = \frac{1}{\omega_r}\sqrt{2E_{pot}/m}$, and angles φ and θ determined by random numbers with probability distributions $P(\varphi) = \frac{1}{2\pi}$, $P(\theta) = \frac{1}{2}sin(\theta)$. Then the cartesian coordinates are determined by:

$$\begin{aligned} x &= r\cos(\varphi)\sin(\theta), \\ y &= r\sin(\varphi)\sin(\theta), \\ z &= \frac{\omega_r}{\omega_z} r cos(\varphi)cos(\theta). \end{aligned} \tag{C.2}$$

The same procedure, with a sphere of radius $r = \sqrt{2E_{kin}/m}$ in velocity space, is applied to obtain the velocity of a particle.

In order to obtain the correct energy distribution a weight is assigned to each particle, which is given by $g(E) = f(E)\rho(E)$. When computing the value of a quantity such as the total kinetic energy, the contribution of each particle is multiplied by its weight. For the

simulations with a cloud of particles that all have the same energy the determinations of particle coordinates in position and velocity space is done the same way as for a thermal cloud, while all weights are set to 1.

Appendix D

Technology Assessment

Most work done on cold atoms and BEC's still is fundamental research, but the development of several technological applications can be foreseen. An application that has already been developed is the atomic fountain, that provides an accurate new time standard. Cold atoms are given a kick upwards by a laser and then fall back due to gravity. This reduces for example the effect of stray magnetic fields, while the atom traverses the same region twice with opposite velocity. An accurate time standard is obtained from an optical transition of the atom. Also, with cold atoms high resolution spectroscopy is possible, while the velocity of the atoms is so small that the effect of the Doppler shift is greatly reduced.

The most promising application of BEC's is the atom laser. The atom laser is made by extracting atoms from a BEC, enabling extremely precise control over the matter beam. Therefore the atom laser might make etching on nanoscale possible. With a BEC it is also possible to perform an accurate gravitational measurement. Local fluctuations in g could be mapped, giving geologists a useful tool to search for for example oil fields. A final application that can be envisioned is in telecommunications. A single-photon optical switch might be produced from a BEC. This would be based on controlling the refractive index of the BEC by optical means. The range of indices that is within reach is unprecedented, the speed of light can be reduced to several meters per second or even stopped completely [42, 43].